Author's Accepted Manuscript


www.elsevier.com

# Wind induced energy-momentum distribution along the Ekman-Stokes layer. Application to the Western Mediterranean Sea climate

J.M. Sayol, A. Orfila, L.-Y. Oey

PII: S0967-0637(15)30092-3
DOI: http://dx.doi.org/10.1016/j.dsr.2016.01.004
Reference: DSRI2575

To appear in: *Deep-Sea Research Part I*

Received date: 20 August 2015
Revised date: 11 December 2015
Accepted date: 27 January 2016

Cite this article as: J.M. Sayol, A. Orfila and L.-Y. Oey, Wind induced energy-momentum distribution along the Ekman-Stokes layer. Application to the Western Mediterranean Sea climate, *Deep-Sea Research Part I* http://dx.doi.org/10.1016/j.dsr.2016.01.004

# Wind induced energy-momentum distribution along the Ekman-Stokes layer. Application to the Western Mediterranean Sea climate.

J.M. Sayol[a,*], A. Orfila[a], L.-Y. Oey[b,c]

[a] *IMEDEA(CSIC-UIB). 07190 Esporles, Balearic Islands, Spain*
[b] *National Central University. Jhongli City, Taoyuan County, Taiwan*
[c] *Princeton University. Princeton, New Jersey, USA*



## Abstract

Wind-wave interaction in the Western Mediterranean Sea is analyzed using 16 years of model data. The mass transport and energy distribution due to wind and waves are integrated through the Ekman-Stokes layer and then spatially and seasonally analyzed. The Stokes drift is estimated from an empirical parameterization accounting for local surface wind and the significant wave height. The impact of the Stokes drift depends on wind variability at the ocean surface and also on the geographical configuration of the basin. The Western Mediterranean Sea has on average a wind energy input two times higher in winter than in summer, and the Stokes-Ekman mass transport interaction term contributes approximately 10% to 15% of the total wind induced transport, but at some locations the contribution is as much as 40% or more.

*Keywords:* Wind-wave interaction, Stokes drift, Ekman-Stokes layer, Mass transport, Wind energy input, Western Mediterranean Sea

*Corresponding author
*Email address:* `jsayol@imedea.uib-csic.es` (J.M. Sayol)

## 1. Introduction

Surface gravity waves have an associated current, the Stokes drift velocity resulting from the non-linearities of the wave orbital velocities (Stokes, 1847). The most accurate way to consider how this wave-induced current interacts to the mean flow is still a subject of ongoing study (see *e.g.* McWilliams et al. (2004); Weber et al. (2006); Mellor (2008)). From the Eulerian standpoint, the Stokes-drift-induced-current is considered an additive term that interacts to the mean ageostrophic current, appearing in the momentum equations as an external force, in the form of a vortex force or as the Coriolis-Stokes force (McWilliams and Restrepo (1999); Smith (2006); Uchiyama et al. (2010)).

Few previous studies estimated the effect of the Stokes drift on energy and mass transport within the Ekman-Stokes layer in real scenarios. Liu et al. (2007) studied at global scale the importance of the Stokes drift interactions in relation to the wind input energy along the Ekman-Stokes layer. They quantified the energy input to the subinertial motions, by deducing an expression for the total wind input in a stationary wave field distinguishing two terms: the direct wind and the wave induced components showing that the wave energy component contributes around 12% in the total (direct wind and wave) energy input. Wu and Liu (2008) studied the energy distribution in the Antarctic Circumpolar Current finding that the wave energy component accounted on average for a 22% of the total energy. Kantha et al. (2009), estimated the role of the Stokes drift as an energy dissipator at a global scale; they pointed out that although the Stokes drift penetrates downwards only a few meters it enhances the turbulence affecting the ocean mixed layer and contributing to the Langmuir circulation. Teixeira (2012) developed a model to obtain the turbulent kinetic energy dissipation injected into the water by breaking waves and subsequently amplified due to its distortion by the mean shear of the wind-induced current and straining by the Stokes drift of surface waves in the same mechanism as the one responsible for the Langmuir circulation. Tamura et al. (2012) estimated the impact of the Stokes drift on the wind induced transport along the Ekman-Stokes layer in the North Pacific ocean, showing that the value of the Stokes-drift computed from the wave significant height and peak period (bulk parameters, *i.e.* statistical estimations) underestimates the real value.

Conversely, the Stokes depth is overestimated by using the bulk expression, which is inversely proportional to the wave number magnitude. The main drawback in the Stokes drift bulk expression is the absence of the local wind in the formulation neglecting the wave-current interaction. On the other hand, the bulk formulation assumes that waves are monochromatic and therefore do not take into account the rapid decay of a real broad wave spectra and overestimates the Stokes e-folding depth (Breivik et al., 2014). Recent global studies have computed directly the Stokes drift at global scale by using the full wave spectra (Harcourt and D'Asaro, 2008) or by using data measured from scatterometers (Liu et al., 2014). Both works focused on the mass transport distribution at the ocean surface analyzing the Stokes drift contribution from wind-sea and swell. Some empirical parameterizations include the local surface wind in the Stokes drift (*e.g.* Li and Garrett (1993), Ardhuin et al. (2009)).

These works pointed out the importance of the effects of waves on the mass transport at the sea surface. For instance, the role of the Stokes drift in the advection of debris in certain regions has been already noticed (Kubota, 1994) as well as the dispersion of buoyant material by Langmuir circulation (Nimmo Smith and Thorpe, 1999; Thorpe, 2009). However, to the best of our knowledge, there are no previous studies quantifying the influence of the Stokes drift in the energy and mass distribution in the Western Mediterranean Sea. In fact, operational models used for Search and Rescue and oil spill operations usually do not include the interaction between wind induced currents and the wave term which is known to contribute for the surface dynamics at the sub mesoscale. In this work we approach the above wind-wave interaction trying to fill the gap in the knwoledge of the processes in the Western Mediterranean Sea by analyzing the vertically integrated mass transport and energy distribution in the upper ocean.

This manuscript is divided as follows: Section 2 presents the dataset (ocean wave model outputs and buoys) and the area of study; in Section 3 the wind induced energy and mass flux formulations are presented; in Section 4 main results are presented and discussed. In section 5 main conclusions and limitations of the methodology are presented together with future work.

## 2. Dataset and Study Area

### *2.1. Wind and Wave model*

The wave model implemented is the third generation spectral wave model WAM (Komen et al., 1994). The model describes the evolution of two-dimensional ocean wave spectra without any assumption on the spectral shape by integrating the 2D transport of action density equation. Wind forcing is a 3-hour wind field from ARPERA, covering 16-year period from January 1$^{st}$ 1993 to December 31$^{st}$ 2008. ARPERA is a multi-decadal wind hindcast from a dynamical downscaling of a coarser climatic model (ERA40). Fields are provided every 3 hours with a spatial resolution of $\sim 0.16°$. Here, we use averaged daily fields centred at 12:00 UTC, being the period covered long enough to capture the seasonal variability. Each model output includes the statistical information of the integrated spectra together with the surface wind velocity information at each grid point. Data analyzed consisted of 5840 daily fields of wind velocity, wind direction, and wave-related statistically averaged magnitudes (also called bulk parameters) such as the significant wave height, wave direction and mean and peak wave period. In addition, model outputs also include some bulk parameters separated by both wind-sea and swell wave components such as the wave significant height, the wave direction and the mean wave period that will be used in Section 4.5. Here we notice that since $\mathrm{T_p}$ is not provided in the model outputs for wind-sea and swell components, we will estimate it by applying the following relationship between the mean ($\mathrm{T_m}$) and the peak period ($\mathrm{T_p}$) for the JONSWAP spectrum,

$$\mathrm{T_p} \approx \frac{\mathrm{T_m}}{1 - 0.532(\gamma + 2.5)^{-0.569}},$$

where $\gamma$ is a factor that determines the concentration of the spectrum on the peak and varies between $[1, 7]$, with a mean value of $\gamma \approx 3$.

### *2.2. Buoys*

Several deep water buoys from the Spanish Harbour Authority -Puertos del Estado- are available within the model domain. Temporal coverage and percentage of gaps differs from buoy to buoy, ranging from a couple of years to about a decade. The location of each buoy is marked with a black circle in Fig. 1. All buoys contain information about several parameters although for this study we only will use the wave significant height ($\mathrm{H_s}$), mean wave period ($\mathrm{T_m}$), wave peak period ($\mathrm{T_p}$) and wind speed ($\mathrm{W_{10}}$). Buoys are distributed across areas with very different ocean and atmospheric dynamics. For instance, the buoy at "Cabo Gata" is placed on the Alboran Sea, very close to the quasi-permanent eastern anticyclonic gyre, a location where the wind direction is highly variable. On the contrary, the buoy at "Cabo Begur" is located in the middle of the Northern Current, where wind usually blows from North or North-West (Tramuntana or Mistral from the local wind names) specially from October to March.

Wave model data were calibrated in a previous work through a Root Mean Square Error (RMSE) minimization process using several buoys in the Western Mediterranean Sea (Martínez-Asensio et al., 2013). The relationship between calibrated and original $\mathrm{H_s}$ is given by $\mathrm{H_s^{cal}} = \alpha {\mathrm{H_s}}^{\beta}$, where $\alpha$ and $\beta$ depend on the model grid point. In short, the calibration corrected a wave model underestimation of $\mathrm{H_s}$.

### *2.3. Area of interest*

WAM simulations cover mainly the Western Mediterranean Sea from 5° W (Strait of Gibraltar) to 15°E (Sicily Channel) (Fig. 1). Surface winds are characterized by a strong seasonality with intense northerly and north-westerly events in the Gulf of Lions during autumn and winter (well-known as Tramuntana and Mistral winds in the Mediterranean region). These winds result in a large fetch area in the Gulf of Lions. Waves propagate from there toward the South-East, reaching the Italian islands of Sardinia and Sicily and the Northern African coast. A secondary area of generation with a small fetch is at the Alboran Sea where strong winds, mainly during summer and autumn blow with large spatial variability. The nearly enclosed topography inhibits waves from propagating far. When westerly wind blows, remote long waves from the North Atlantic region enter through the Strait of Gibraltar.

## 3. Methods

### *3.1. Ekman-Stokes layer solution: Vertically integrated transport*

To analyze the effects of surface waves into the Ekman layer we average the momentum equations over wave periods considering a stationary flow in a slowly varying wave field (McWilliams et al., 1997; Lewis and Belcher, 2004; Polton et al., 2005). Under these conditions, the ageostrophic motions are governed by,

$$\rho_w \mathrm{f}\, \hat{\mathbf{k}} \times (\mathbf{u} + \mathbf{u_s}) = \frac{\partial}{\partial z}\left(\kappa \frac{\partial \mathbf{u}}{\partial z}\right), \tag{1}$$

being $\rho_w$ the seawater density, f the Coriolis parameter, $\hat{k}$ the unit vector in the z-direction, $\kappa$ a constant vertical viscosity and where the Stokes-Coriolis force, $\mathrm{f}\hat{\mathbf{k}} \times \mathbf{u_s}$ has been added to the Ekman model of the mean velocity $\mathbf{u}$. The classical assumption of constant $\kappa$ has strong implications on the Ekman transport, restricting the Ekman spiral shape. In particular the surface Ekman current is forced to 45° to the right of the surface wind and the Ekman vertically integrated transport is directed 90° to the right of the surface wind (for the Northern Hemisphere case, to the left in the Southern Hemisphere) (Ekman, 1905). This approach is only acceptable for deep ocean (*i.e.* ocean depth >> Ekman depth) because $\kappa$ cancels when integrating along the whole Ekman spiral. For the sake of clarity, the Ekman depth is usually defined as the depth at which the Ekman current have turned 180° relative to the direction at the surface. Adopting the complex form for the velocity vectors and assuming monochromatic waves, *i.e.*,

$$\mathbf{u}_s = u_s^x + iu_s^y = \mathrm{U_s}\, \mathrm{e}^{i\theta_w} \mathrm{e}^{z/\delta_{\mathrm{St}}} \equiv \mathcal{U}_s,$$

$$\mathbf{u} = u^x + iu^y \equiv \mathcal{U},$$

Eq. (1) can be rewritten as,

$$\frac{\partial^2 \mathcal{U}}{\partial z^2} - \mathrm{a}\mathcal{U} = \mathrm{a}\mathcal{U}_s, \tag{2}$$

where $\mathrm{a} = i\,(\mathrm{f}/\kappa)$ and $\delta_{\mathrm{St}}$ being the Stokes e-folding depth (the depth at which Stokes drift current has decayed e) and $\theta_w$ the angle of waves measured counterclockwise from the west-east direction. The following boundary conditions apply for the mean flow,

$$\frac{\partial \mathcal{U}}{\partial z} = \frac{|\boldsymbol{\tau}|}{\kappa \rho_w} \mathrm{e}^{i\theta_u^{10}} \qquad \text{at} \qquad \mathrm{z} = 0 \tag{3}$$

$$\mathcal{U} = 0 \qquad \text{at} \qquad \mathrm{z}/\delta_{\mathrm{St}} \text{ and } \mathrm{z}/\delta_{\mathrm{Ek}} = -\infty \tag{4}$$

where $\theta_u^{10}$ is the angle of the wind measured counterclockwise from the west-east direction and $\delta_{\mathrm{Ek}}$ is the Ekman depth. The solution for the two-point boundary value problem of Eq. (2) subjected to (3)-(4) is:

$$\begin{aligned}\mathcal{U}(z) = \mathrm{e}^{\frac{(1+i)z}{\delta_{\mathrm{Ek}}}} \left\{ \frac{(1-i)|\boldsymbol{\tau}|\mathrm{e}^{i\theta_u^{10}}}{\rho_w \mathrm{f}\, \delta_{\mathrm{Ek}}} + \mathrm{U_s} \mathrm{e}^{i\theta_w} c \left( \frac{(2-c^2) - i(2+c^2)}{c^4+4} \right) \right\} + \\ + 2\mathrm{U_s}\mathrm{e}^{i\theta_w} \mathrm{e}^{z/\delta_{\mathrm{St}}} \left( \frac{ic^2 - 2}{4 + c^4} \right)\end{aligned} \tag{5}$$

where $c = \delta_{\mathrm{Ek}}/\delta_{\mathrm{St}}$ is the non-dimensional Ekman - Stokes number. The first term in Equation (5) is the Ekman current which can be rewritten in trigonometric form as (see *e.g.* Pond and Pickard (1983)),

$$\begin{aligned} \mathrm{U_{Ek}} = &\quad V_0 \cos\left(\theta_u^{10} - \pi\left[1/4 + |z|/\delta_{\mathrm{Ek}}\right]\right) \mathrm{e}^{z/\delta_{\mathrm{Ek}}} \\ \mathrm{V_{Ek}} = &\quad V_0 \sin\left(\theta_u^{10} - \pi\left[1/4 + |z|/\delta_{\mathrm{Ek}}\right]\right) \mathrm{e}^{z/\delta_{\mathrm{Ek}}} \end{aligned} \tag{6}$$

where $(\mathrm{U_{Ek}}, \mathrm{V_{Ek}})$ are defined for $z \leq 0$ and for the Northern Hemisphere. In Eq. (6), $V_0 = \dfrac{\sqrt{2}|\boldsymbol{\tau}|}{\delta_{\mathrm{Ek}}\rho_w|\mathrm{f}|}$ is the Ekman current amplitude and $|\boldsymbol{\tau}|$ is the modulus of the wind stress. For typical values in the Mediterranean Sea as

$|\boldsymbol{\tau}| = 0.1\,\mathrm{N/m^2}$, $\delta_{\mathrm{Ek}} = 30\,\mathrm{m}$, $\mathrm{f} = 10^{-4}\,\mathrm{s^{-1}}$, $\rho_w = 1029\,\mathrm{kg/m^3}$, the surface Ekman currents amplitude take a value of $V_0 \approx 4.5\,\mathrm{cm/s}$.

The total transport in the Ekman-Stokes layer can be expressed in complex notation $\mathcal{M}$ as,

$$\mathcal{M} = \int_{-\infty}^{0} \mathcal{U}(z)\,dz = \mathbf{M}^{\mathrm{Ek}} + \mathbf{M}^{\mathrm{St-Ek}} + \mathbf{M}^{\mathrm{St}}, \tag{7}$$

where,

$$\begin{aligned}
\mathbf{M}^{\mathrm{Ek}} &= \frac{-i|\boldsymbol{\tau}|}{\mathrm{f}\rho_w}\mathrm{e}^{i\theta_u^{10}} \\
\mathbf{M}^{\mathrm{St-Ek}} &= \frac{(1-i)}{2}c^2(\mathrm{U_s}\delta_{\mathrm{St}})\mathrm{e}^{i\theta_w}\frac{\left[(2-c^2)-i(2+c^2)\right]}{c^4+4} \\
\mathbf{M}^{\mathrm{St}} &= 2\mathrm{U_s}\delta_{\mathrm{St}}\mathrm{e}^{i\theta_w}\frac{(ic^2-2)}{4+c^4}
\end{aligned}$$

The zonal and meridional transport are $M_x = \mathfrak{Re}\{\mathcal{M}\}$ and $M_y = \mathfrak{Im}\{\mathcal{M}\}$. The first term, $\mathbf{M}^{\mathrm{Ek}}$ is the vertically integrated wind induced Ekman transport, with a net transport of 90° to the right of the surface wind. The second term, $\mathrm{M}^{\mathrm{St-Ek}}$ is the integrated transport resulting from the interaction between the Stokes-drift and the wind-induced current, while the third term, $\mathbf{M}^{\mathrm{St}}$ is the Stokes transport due to the non-linear advection induced by waves.

To show the contribution of the terms that do not appear in the classical Ekman solution, Fig. 2 shows the theoretical distribution of $|\mathbf{M}^{\mathrm{St}}|^2 = \dfrac{4(\mathrm{U_s}\delta_{\mathrm{St}})^2}{4+c^4}$ (red line) and $|\mathbf{M}^{\mathrm{St-Ek}}|^2 = \dfrac{c^4\,(\mathrm{U_s}\delta_{\mathrm{St}})^2}{(4+c^4)}$ (blue line) as a function of $c$. Also the addition of both terms is shown for completeness (black line). As seen in Fig. 2 as $c$ increases, the Stokes component (red line) reduces whereas the Stokes-wind term increases (blue line). In the absence of wind, the Stokes-Ekman term is zero so as $\delta_{\mathrm{Ek}} = c = 0$ cancels, whereas the Stokes term will be the only contribution if waves are present, $\lim_{c\to 0}|\mathbf{M}^{\mathrm{St}}|^2 = (\mathrm{U_s}\delta_{\mathrm{St}})^2$.

As wind increases, the Ekman layer develops and $c$ arises. At $c = \sqrt{2}$ the sum of the Stokes and Stokes-Ekman terms is maximum (sea black line). At this point the Ekman spiral is affected by the surface waves while the wave induced mass flux remains high. After this point the Stokes mass transport decays up to $c \sim 4$, where almost the asymptotic limit is reached: $\lim_{c\to\infty} |\mathbf{M}^{\mathrm{St-Ek}}|^2 = (\mathrm{U_s}\delta_{\mathrm{St}})^2$. Contrarily, if $c >>$ the Stokes drift term becomes negligible respect to the Stokes-wind term and almost all mass transport results from the interaction between Stokes drift and the Ekman current. Considering that wind is ubiquitous in the real ocean -except in some limited areas such as the equatorial regions-, the Ekman depth is always there being larger than the Stokes depth.

### *3.2. Ekman-Stokes layer solution: Wind induced integrated energy*

The energy distribution in the Ekman-Stokes layer can be readily obtained following Liu et al. (2007) and Wu and Liu (2008) by multiplying both sides of Eq. (1) by $\mathbf{u}$ and averaging over a wave period. Polton (2009) introduced a correction in the formulation by including an extra term accounting for the correlations between the Stokes-Coriolis and the mean current shear. Additionally, the expression of the vertically integrated energy was rewritten in terms of the surface Stokes drift and the wind stress for the case of a steady wave field. Hereinafter we will use Polton's approach to compute the energy rate balance assuming a steady field. The total wave-averaged, depth-integrated energy is decomposed into wind-induced ($\mathrm{E_w}$, mainly Ekman currents) and wave-induced ($\mathrm{E_s}$, mainly Stokes drift) components so as

$\mathrm{E} = \mathrm{E_w} + \mathrm{E_s}$ and being,

$$\mathrm{E_w} = \frac{|\boldsymbol{\tau}_0|^2}{\rho\delta_{\mathrm{Ek}}\mathrm{f}} + \boldsymbol{\tau}_0 \times \mathrm{U}_{s_0}\,\hat{\mathbf{k}}\,F_2(c) - \boldsymbol{\tau}_0 \cdot \mathrm{U}_{s_0}\,F_1(c) \tag{8}$$

$$\mathrm{E_s} = \frac{1}{c}\left[\rho_w \mathrm{f}\delta_{\mathrm{Ek}}|\mathrm{U}_{s_0}|^2 F_2(c) + \boldsymbol{\tau}_0 \cdot \mathrm{U}_{s_0} + \boldsymbol{\tau}_0 \times \mathrm{U}_{s_0}\,\hat{\mathbf{k}}\right] \tag{9}$$

where $F_1(c) = \dfrac{c+2}{(c+1)^2+1}$ and $F_2(c) = \dfrac{c}{(c+1)^2+1}$. The surface wind stress is empirically obtained as a function of the wind velocity at 10 m height, $\mathrm{W}_{10}$ as $|\boldsymbol{\tau}_0| = \rho_a C_d \mathrm{W}_{10}^2$ whereas the drag coefficient is $C_d = (0.75 + 0.067\,\mathrm{W}_{10}) \cdot 10^{-3}$ (Li and Garrett, 1993). The air density is constant and taken in this work as $\rho_a = 1.2\,\mathrm{kg/m^3}$, whereas seawater density is $\rho_w = 1029\,\mathrm{kg/m^3}$ (the average value for the Mediterranean Sea).

In this simplified model the wind energy input per unit of time and area (units in $\mathrm{W \cdot m^{-2}}$) (the so-called energy rate in Polton (2009)), can be decomposed in two contributions ($\mathrm{E_w}$ and $\mathrm{E_s}$) the first accounting for the wind-induced energy used to generate currents (first term in Eq. 8) and the energy exchange with waves (second and third terms in Eq. 8) and the second related with waves (indirect wind energy), where the first term in Eq. 9 represents the wave-induced Stokes drift and the other two terms result from the interaction between the Stokes drift and the surface wind. All possible combinations derived from the relative angle between wind and waves are shown in Fig. 3 where parameters and variables in Eq. 8 and Eq. 9 have been taken as constant (see caption of Fig. 3 for more details). From this figure we can notice that E and $\mathrm{E_w}$ are always positive whereas that $\mathrm{E_s}$ can be negative. Note that the second and third terms in both $\mathrm{E_w}$ and $\mathrm{E_s}$ redistribute the energy from wind to waves or viceversa. From Fig. 3 we see that E is maximum when the angle between wind and waves is $\theta = 90°$ (clockwise notation) whereas $\mathrm{E_w}$ is maximum for $\theta = 135°$ and the maximum for $\mathrm{E_s}$ corresponds to $\theta = 45°$. This is explained as follows; $E_s$ is more favored when waves move parallel to the surface Ekman current ($\theta = 45°$) since it can be reinforced receiving energy from wind. The opposite occurs when ($\theta = 225°$) since wind (Ekman current) block wave propagation. If $\theta = 90°$ the total energy increases because the vertically integrated Ekman transport is parallel to waves and momentum can be transferred from waves downwards the Ekman layer. On the other hand, waves can extract less energy from wind. Finally, if $\theta = 135°$ waves cannot take energy from wind but they reinforce the Ekman transport being all energy available for $E_w$. The role of the Stokes-Coriolis term is therefore to redistribute the energy through the Ekman-Stokes layer but not contributing to a net energy production. The above energy balance only accounts for the energy budget below the troughs as already pointed out by Polton (2009).

### *3.3. Stokes drift estimation*

For irrotational waves propagating in deep waters (*i.e.* $kh > \pi$ where $k = |\mathbf{k}| \equiv |k(\cos\theta, \sin\theta)|$ is the wave number and $h$ the local water depth), the bulk Stokes drift at the surface is (Longuet-Higgins, 1953),

$$\mathrm{U_s^b} = g^{-1}\omega_p^3 a^2 \tag{10}$$

where $g$ is acceleration of gravity, $a \equiv \mathrm{H_s}/2\sqrt{2}$ the wave amplitude and $\omega_p = 2\pi/\mathrm{T_p}$ the frequency at the peak period. Eq. (10) is valid for harmonic waves.

Ardhuin et al. (2009) obtained two parameterizations to compute the Stokes drift velocity based on model and buoy data that, contrary to the bulk expression, include the local surface wind effect ($\mathrm{W_{10}}$). These expressions are for buoy and model data respectively:

$$\mathrm{U}^{\mathrm{Ad}}_{\mathrm{s_b}} = 5.9 \cdot 10^{-4} \left( 1.25 - 0.25 \left( \frac{0.5}{f_c} \right)^{1.3} \right) \mathrm{W}_{10}\mathrm{W}^{m}_{10} + 0.027\,(\mathrm{H_s} - 0.4)\,,$$

$$\mathrm{U}^{\mathrm{Ad}}_{\mathrm{s_m}} = 5 \cdot 10^{-4} \left( 1.25 - 0.25 \left( \frac{0.5}{f_c} \right)^{1.3} \right) \mathrm{W}_{10}\mathrm{W}^{m}_{10} + 0.025\,(\mathrm{H_s} - 0.4)\,, \quad (11)$$

where $f_c$ refers to the cut-off frequency ($\sim 0.5\,\mathrm{Hz}$ from buoys), and $\mathrm{W}^{m}_{10}$ imposes an upper threshold for wind data that can be expressed as follows:

$$\mathrm{W}^{m}_{10} = \begin{cases} \mathrm{W}_{10} & \text{if } \mathrm{W}_{10} < 14.5\ [m\,s^{-1}], \\ 14.5 & \text{if } \mathrm{W}_{10} \geq 14.5\ [m\,s^{-1}]. \end{cases}$$

Then:

$$\mathbf{U}^{\mathrm{Ad}}_{\mathrm{s}}(z) = \mathrm{U}^{\mathrm{Ad}}_{\mathrm{s,0}}\, \mathrm{e}^{z/\delta_{\mathrm{St}}} \left[ \cos(\theta_w)\hat{\mathbf{i}} + \sin(\theta_w)\hat{\mathbf{j}} \right] \quad (12)$$

### *3.4. Ekman-Stokes layer depths*

*Stokes depth*

The Stokes e-folding depth layer expression for a developed, stationary, and deep water monochromatic wave can be obtained from the Stokes drift exponential decay,

$$\mathrm{U_s} = \mathrm{U_s}(0)\mathrm{e}^{2kz}.$$

where the subscript b denoting "bulk" expression has been omitted for clarity. Setting $\delta_{\mathrm{St}}$ to be where $\mathrm{U_s}$ decays to $\mathrm{U_s}(0)/\mathrm{e}$, we have $\delta_{\mathrm{St}} = 1/2\,k$. For deep water wave, *i.e.* $\omega^2 = g\,k$, the Stokes depth expressed with bulk parameters is, $\delta^{Bulk}_{\mathrm{St}} = g/(2\,\omega^2)$. However, as shown by Tamura et al. (2012) (see their Fig. 1) this expression overestimates the Stokes depth. In fact, Breivik et al. (2014) stated that the bulk expression: "*. . . it is clear that the shear under a broad spectrum is much stronger than that of a monochromatic wave of intermediate wavenumber due to the presence of short waves whose associated Stokes drift quickly vanishes with depth. At the same time, the deep*

*Stokes drift profile will be stronger than that of a monochromatic wave since the low-wavenumber components penetrate much deeper*". In this context these authors proposed a modified vertical profile for the Stokes drift that approaches the exponential shape near the surface and goes as an asymptotic solution in the deep, as,

$$\mathrm{U_s}^c = \mathrm{U_s}(0)\,\frac{e^{2\,k_e z}}{1 - C\,k_e z},$$

being $k_e \sim k/3$ and $C \sim 8$. For $\mathrm{U_s}^c = \mathrm{U_s}(0)/\mathrm{e}$ the e-folding depth is the root of the non-linear equation,

$$\delta_{\mathrm{St}} - \frac{\log\left(1 - 8k_e\delta_{\mathrm{St}}\right) - 1}{2k_e} = 0, \tag{13}$$

that can be solved numerically.

*Ekman Depth*

The Ekman depth can be expressed empirically as (see Csanady (1982) and Wu and Liu (2008)), $\delta_{\mathrm{Ek}} = \epsilon u_w^*/\mathrm{f}$, where $u_w^*$ is the friction velocity $u_w^* = \sqrt{|\boldsymbol{\tau}_0|/\rho_w}$, and $\epsilon$ is a non-dimensional constant $\approx 0.38$.

Let $u_a^* = \sqrt{|\boldsymbol{\tau}_0|/\rho_a} = \sqrt{C_d}\,\mathrm{W}_{10}$, we obtain,

$$\delta_{\mathrm{Ek}} \simeq 0.38\frac{\mathrm{W}_{10}}{\mathrm{f}}\sqrt{\frac{C_d\rho_a}{\rho_w}}, \tag{14}$$

which will be used in this work.

*3.5. Stokes drift decomposition: wind-sea and swell*

As a first approach the Stokes drift can be linearly decomposed as (see *e.g.* McWilliams et al. (2013)),

$$\mathbf{U}_{\mathrm{St}} = \mathbf{U}_{\mathrm{St}}^{\mathrm{sea}} + \mathbf{U}_{\mathrm{St}}^{\mathrm{swell}}, \tag{15}$$

where it has been assumed that wind-sea and swell spectra are separable, with a marked different period resulting in a much narrower spectra for swell waves.

Previous works have estimated the Stokes drift separately for wind-sea and swell wave components by separating the spectrum through the definition of a threshold frequency (for a more complete explanation of the method read Bidlot (2001)). However, due to the unavailability of the full spectra we are forced to estimate wind-sea and swell Stokes drift components directly from the wave model bulk parameters presented in Section 2.1. Thus, in this work the Stokes drift wind-sea component, $\mathrm{U}_{\mathrm{St}}^{\mathrm{sea}}$ is computed using the Ardhuin parametrization (Eq. (11), because of the wind-sea dependence on local wind) whereas the swell component, $\mathrm{U}_{\mathrm{St}}^{\mathrm{swell}}$ is computed using the bulk approach (Eq. (10), swell waves are by definition independent of local wind). This division between wind-sea and swell when using the wave model output parameters is not very accurate as will be shown later. However, it is useful to better characterize spatially and seasonally if a region is more influenced by local wind waves or by remote swell waves.

If the Stokes drift is linearly decomposed as presented in Eq. (15), the solution of the Stokes-Ekman layer (Eq. 7) reads,

$$\mathbf{M} = \int_{-\infty}^{0} \mathcal{U}(z)\, dz = \mathbf{M}_{\mathrm{Ek}} + \mathbf{M}_{\mathrm{St-Ek}}^{\mathrm{sea}} + \mathbf{M}_{\mathrm{St-Ek}}^{\mathrm{swell}} + \mathbf{M}_{\mathrm{St}}^{\mathrm{sea}} + \mathbf{M}_{\mathrm{St}}^{\mathrm{swell}}, \qquad (16)$$

where the different terms given by,

$$
\begin{aligned}
\mathbf{M}_{\mathrm{Ek}} &= \frac{-i|\boldsymbol{\tau}|}{\mathrm{f}\rho_w}\mathrm{e}^{i\theta_u^{10}} \\
\mathbf{M}_{\mathrm{St-Ek}}^{\mathrm{sea}} &= \mathrm{U}^{\mathrm{sea}}\delta_{\mathrm{Ek}}\mathrm{e}^{i\theta^{\mathrm{sea}}}\frac{(1-i)}{2}c_{\mathrm{sea}}\frac{\left(2-c_{\mathrm{sea}}^2\right)-i\left(2+c_{\mathrm{sea}}^2\right)}{4+c_{\mathrm{sea}}^4} \\
\mathbf{M}_{\mathrm{St-Ek}}^{\mathrm{swell}} &= \mathrm{U}^{\mathrm{swell}}\delta_{\mathrm{Ek}}\mathrm{e}^{i\theta^{\mathrm{swell}}}\frac{(1-i)}{2}c_{\mathrm{swell}}\frac{\left(2-c_{\mathrm{swell}}^2\right)-i\left(2+c_{\mathrm{swell}}^2\right)}{4+c_{\mathrm{swell}}^4} \\
\mathbf{M}_{\mathrm{St}}^{\mathrm{sea}} &= 2\mathrm{U}^{\mathrm{sea}}\mathrm{e}^{i\theta^{\mathrm{sea}}}\delta_{\mathrm{St}}^{\mathrm{sea}}\frac{\left(ic_{\mathrm{sea}}^2-2\right)}{4+c_{\mathrm{sea}}^4} \\
\mathbf{M}_{\mathrm{St}}^{\mathrm{swell}} &= 2\mathrm{U}^{\mathrm{swell}}\mathrm{e}^{i\theta^{\mathrm{swell}}}\delta_{\mathrm{St}}^{\mathrm{swell}}\frac{\left(ic_{\mathrm{swell}}^2-2\right)}{4+c_{\mathrm{swell}}^4},
\end{aligned}
\tag{17}
$$

where $c_{\mathrm{sea}} = \delta_{\mathrm{Ek}}/\delta_{\mathrm{St}}^{\mathrm{sea}}$ and $c_{\mathrm{swell}} = \delta_{\mathrm{Ek}}/\delta_{\mathrm{St}}^{\mathrm{swell}}$, where $c_{\mathrm{sea}}$ and $c_{\mathrm{swell}}$ refer to the Ekman-Stokes numbers and $\delta_{\mathrm{St}}^{\mathrm{sea}}$ and $\delta_{\mathrm{St}}^{\mathrm{swell}}$ are the Stokes e-folding depths for wind-sea and swell terms. Both depths have been estimated following Eq. 13 by using the wave parameters for wind-sea and swell introduced in Section 2.1 (mean wave direction, mean wave significant height and mean wave period).

## 4. Results and Discussion

### *4.1. Stokes drift estimation*

The Stokes-drift computed for the deep-water buoys (see locations in Fig. 1) and wave model are compared in Table 1 with the statistical parameters defined in Appendix 1. The table shows the values of the Stokes drift computed using the calibrated value of $\mathrm{H_s}$ (see Section 2.2) as well as the non-calibrated value. Moreover, Stokes drift for both sets of data is computed using the bulk formulation and the Ardhuin parametrization (Eq. (11)). The most significant results that can be inferred from the Table 1 are:

- Stokes drift computed from the bulk expression is 50% smaller than the one computed from the Ardhuin formulation,
- when using the Ardhuin expression, the correlation coefficients (CC) between buoy and model data are substantially higher and the scatter index (SI) a 50% lower, showing that results are less dispersed,
- the calibration deteriorates the Stokes drift estimations when using the bulk formulation, increasing the root mean square error (RMSE) as well as the dispersion (SI) and reducing the CC. A calibration of $T_p$ may also be necessary in order to improve the Stokes drift computation, which is beyond the scope of this paper.

Estimation of the Stokes drift velocity using Eq. 10 or Eq. 11 requires accurate measurements of $H_s$, $T_p$ and $W_{10}$. Tamura et al. (2012) compared the Stokes drift velocity from wave model data and *in situ* measurements with several buoys in the North Pacific by using different methods, *i.e.*: integrating the model spectra, applying the wave bulk values Eq. (10) and finally, using empirical parameterizations. They found that the Stokes drift was systematically underestimated when using the bulk formulation, which is based on the wave statistical estimators, $H_s$ and $T_p$. In fact, they found a much better agreement with the buoys if the spectrum was fully integrated or when using empirical parametrizations rather than the bulk expression. In more detail, together with the integration of the spectra, the use of the parametrization of Ardhuin (either for buoy or model) turned out to be the best approach. By including the local wind effect in computing the Stokes drift, as is done in the Ardhuin expression, dispersion and RMSE are reduced significantly, while correlation between buoys and model increased dramatically.

The comparison provided in Table 1 is in agreement with the results of Tamura et al. (2012), confirming that the inclusion of the local wind, is critical to reproduce accurately the Stokes drift current. Despite this, Stokes drift estimated from model data tends to be underestimated compared to buoys. The distribution of calibrated (red dots) and non-calibrated (blue dots) Stokes drift velocities for each buoy is shown in Fig. 4. As seen, the Stokes drift velocity dispersion and magnitude varies greatly from buoy to buoy, reaching in some places as "Maó" and "Cabo Gata" values over 0.15 m/s, being of the order (or even higher) than the geostrophic currents -given for instance in Fig. 8 of Poulain et al. (2012)-. Fig. 4 also shows the linear least squares fit for calibrated (solid orange line) and non-calibrated data (solid cyan line). In the remaining part of this paper, unless otherwise stated, Stokes drift velocity will be computed using the Ardhuin formulation with calibrated model data.

The seasonal behavior of the Stokes drift velocity is assessed by analyzing its spatial distribution during winter (December-January-February) and summer (June-July-August) seasons (hereinafter DJF and JJA respectively). Fig. 5, top panels display the averaged Stokes drift at surface (black arrows) for DJF (left) and for JJA (right). Background color represents the angular deviation (in degrees) between the direction of the averaged surface wind fields (at 10 m) and the direction of the Stokes drift for the same periods. Positive angular deviations indicate that wind is blowing to the left of the Stokes drift whereas negative angular deviations indicate that wind blows to the right of the surface Stokes drift. The magnitude of the Stokes drift during winter doubles the value obtained during summer (maxima in winter are around $\sim 10\,\text{cm/s}$). Over the shelf of Italy and Spain wind and waves are on average in the opposite direction during winter. The central and bottom rows in Fig. 5, represent winter and summer mean Stokes drift and angular deviations for the sea and swell Stokes drift components. The wind-sea component is much larger than the swell mainly around the generation area. However, in coastal areas the swell component can become large.

### *4.2. Ekman-Stokes layer estimation*

The upper ocean depth where wind and wave induced currents interact to each other is known as the Ekman-Stokes layer. Other interactions can occur near the surface such as the formation of the Langmuir cells. However our numerical model does not resolve these small scale structures.

The averaged Ekman depth, $\delta_{\mathrm{Ek}}$, for the analyzed period is displayed in Fig. 6, top left. Values of the Ekman layer range from 15 m in coastal areas to maxima around 40 m in the middle of the Gulf of Lions, a region characterized by strong winds blowing all year round (fetch region) and more intensely in late fall and winter (Ponce de León et al., 2016). As stated above the Stokes depth, $\delta_{\mathrm{St}}$, when computed through bulk parametrization overestimates the values more accurately estimated in other regions by previous works. The result of correcting the Stokes e-folding depth at each grid point is shown in Fig. 6 (top-right). As observed, the depth increases to the south with a clear gradient oriented with the direction of the main northerly winds with maximum values starting at the lee of Menorca Island.

Values for the Stokes depth are significantly improved when applying the Breivik correction as shown in Table 2. Temporal averaged Stokes depth in the whole basin is reduced to 0.6 m and the median diminishes 0.5 m approaching to the values of $1-3$ m given in the literature (see for instance Tamura et al. (2012); Breivik et al. (2014)).

Solution of Eq. (13) is also used to obtain the wind-sea Stokes depth, $\delta_{\mathrm{St}}^{\mathrm{sea}}$ and the swell Stokes depth, $\delta_{\mathrm{St}}^{\mathrm{swell}}$ both displayed in Fig. 6. As seen, the averaged wind-sea Stokes depth layer takes values between $1-3\,\mathrm{m}$, while the swell Stokes layer depth can be around 10 m (see Fig. 6 (bottom panels)). The higher depth for swell component is because its larger wavelengths that penetrate deeper into the ocean.

### *4.3. Wind Induced Energy Distribution*

Following the energy rate decomposition presented in Section 3.2 and in Fig. 3, we estimate the wind induced energy, $\mathrm{E_w}$, the wave induced energy, $\mathrm{E_s}$ and the total wind energy, $\mathrm{E} = \mathrm{E_w} + \mathrm{E_s}$. These terms explain how wind energy is distributed along the Ekman-Stokes layer under a stationary wave field and assuming no dissipation mechanisms. In addition, cross terms involving wave-wind interaction (or wind-wave) are also considered (see Eq. (8) and Eq. (9)).

The mean total energy for DJF (left) and JJA (right) are depicted in the top panels of Fig. 7. The background color represents the wind energy input per unit of area and time ($\mathrm{W\,m^{-2}}$). Most of the energy is concentrated in the Gulf of Lions, with values during winter near $10^{-2}\,\mathrm{W\,m^{-2}}$ (Fig. 7, top-left). Energy contours present a similar distribution as the Stokes drift (Fig. 5, top left) since waves with larger wavelengths arrive to the North African coast (mainly coasts of Algeria and Tunisia) unimpeded by islands or land intrusions between the Gulf of Lions and the coast. Energy values decrease drastically during summer with maxima around $3 \cdot 10^{-3}\,\mathrm{W\,m^{-2}}$. During summer the wind energy input in the Alboran Sea is as important as the input of energy in the Gulf of Lions.

Energy components for wind and waves are different (second and third row panels of Fig. 7). Wind energy primarily produces Ekman currents (Fig. 7, second row, left column for DJF). The energy contribution from waves is much smaller, as it is especially during JJA with maxima located far from the storm generation area indicating that the cyclogenetic events during this season have less duration and intensity. The ratio between the wave induced energy and the total energy is $\sim 0.3$ (see Fig. 7, bottom left) which suggests that waves are important as an energy input mechanism in the upper water column. This energy ratio decreases in summer to a $10\% - 15\%$. According to Fig. 3 variations in the wave induced energy are due to two reasons: a higher relative angle between local wind and waves and, variations in the Stokes drift due to wind seasonality. Positive $\mathrm{E_s}$ values indicate that the angle between wind and waves are in between $[-45°, 135°]$, which is mainly occurring in the middle of the basin when wind and waves are more aligned (see Fig. 5, top-left). $\mathrm{E_s}$ can be also zero at locations where the angle between wind and waves is very variable (more common in coastal areas). For instance it is the case of the Alboran Sea where the rate of $\mathrm{E_s}$ to E is very low (Fig. 7, bottom panels).

Here we notice that, following the work of, *e.g.* D'Ortenzio et al. (2005), Ekman depth in summer can be much shallower due to the upward displacement of the mixed layer, inhibiting the downward wind-induced momentum and thus, blocking the Ekman currents. This effect enhances the seasonal variability modifying the relative importance of the Stokes drift contribution during summer.

Monthly averaged values (for the whole basin) are shown in Fig. 8 for the total energy rate (top panel), for the wind induced energy rate (middle panel) and for the wave induced energy rate (bottom panel). In the box plots the star refers to the mean and the horizontal line inside the boxes represents the median, whose value is indicated on the top of each box. All energy terms show a marked seasonal behavior with maxima in December/January and minima during July/August given by the variability of energy input at the ocean surface along the year. Box plot size increases during winter with maximum values spatially localized with a large variability along the basin. These results are in accordance with the ones obtained by Wu and Liu (2008), who found that wave induced energy was above 20% of the total wind energy input in the Antarctic Circumpolar Current, and therefore of potential importance that has to be considered in ocean transport analysis.

### *4.4. Wind Induced Mass Flux*

In this section the Stokes layer momentum solution (see Section 3.1) is analyzed in order to study the mass transport $\mathbf{M} = \mathbf{M}_{\mathrm{Ek}} + \mathbf{M}_{\mathrm{St-Ek}} + \mathbf{M}_{\mathrm{St}}$ (see Eq. 7). Fig. 9, top panel, shows the averaged $\mathbf{M}$ in the Ekman-Stokes layer for DJF (left) and JJA (right) where the arrow length indicates the mass flux in $\mathrm{m^2\,s^{-1}}$. Maxima during winter are around $4.0\,\mathrm{m^2\,s^{-1}}$ while during summer is of $1.5\,\mathrm{m^2\,s^{-1}}$. During DJF the averaged mass transport is towards the south/south-west being in JJA season anticyclonically deflected. Second and third rows in Fig. 9 display respectively the Ekman and Stokes components of the mass flux. The Ekman component clearly dominates the total mass transport, being two orders of magnitude larger than the Stokes transport. Mean Ekman transport is deflected around 90° rightward to the surface wind direction following the classical Ekman solution. However, the effects of waves produces a slight change in direction of the total mass transport. The Stokes-Ekman interaction term is depicted for DJF and JJA in the fourth row. Although this term is one order of magnitude smaller than the Ekman contribution is larger than the pure Stokes term contributing on average for an $\sim 15\%$ of the total transport and is directed mostly to the south-east following the wind dominant direction. The median ratio between the Stokes mass transport terms and the total mass transport is depicted in Fig. 9, bottom panels, showing that the Stokes terms are much more important in DJF than in JJA (about 2-3 times larger) and that in some locations this contribution can be as high as 40% of the total mass flux.

The above spatial mass transport distribution is further analyzed by computing the modulus of the monthly transport as well as the Ekman, the Stokes and the combined Stokes-Ekman terms (Fig. 10). Box plots are computed by averaging the whole basin. Roughly, comparison between the different contributions provides $|\mathrm{M_{Ek}}| \sim 10|\mathrm{M_{St-Ek}}| \sim 100|\mathrm{M_{St}}|$. Besides the seasonality in the transport, it is noticeable that during winter, variance is larger because of the large differences in transport in the basin. Stokes transport during March and April remains practically constant or slightly increases during April (see third panel in Fig. 10). This is due to the spring storms affecting the Mediterranean Sea during this month.

### *4.5. Mass flux for wind-sea and swell terms*

In this work we assumed that the Stokes drift can be described by the linear combination of wind-sea and swell Stokes drift components (see Eq. 15, Section 3.5). To infer the validity in this assumption, we compute the RMSE of the Stokes drift (Fig. 11, top panel) and the variance for the zonal and meridional velocity components independently (Fig. 11, central and bottom panels respectively) for DJF (left) and JJA (right) seasons. The mean RMSE value is about 1 cm/s at basin scale during summer, and 2 cm/s during winter. RMSE is larger in the middle of the basin, mainly in the North African coast around the longitude of $5^\circ$ E. In fact, the highest

RMSE is explained by the maximum variance in the meridional component (Fig. 11, bottom left).

The total mass transport and the contribution of each of the above described components for the Stokes (sea and swell) and the Stokes-Ekman (sea and swell) mass transport are shown in Fig. 12 (note that the pure Ekman transport is the same as in Fig. 9 and therefore not repeated). By this decomposition the total mass transport (Fig. 12, top panels) is slightly larger than the one obtained previously (Fig. 9, top panels). The pure Stokes component is dominated by the swell contribution ($60 - 70\%$) (Fig. 12, middle panels). The Stokes mass transport component shows, specially during DJF, a similar spatial pattern than the provided by the swell (compare Fig. 9, middle-left panel and Fig. 12, middle-left panel). Contrarily, the Stokes-Ekman interaction term is clearly dominated by the wind-sea component with a contribution of over 90% in the mass transport (compare Fig. 12, fourth and fifth rows). Recently, Carrasco et al. (2014) studied separately wind-sea and swell mass flux distribution at global scale for more than 50 years of data using a wave model reanalysis. These authors found that the swell dominates the transport around the equatorial ocean where winds are weak (these regions are called "swell pools" following references therein).

Seasonality of the above presented magnitudes are presented in Fig. 13 for the total modulus of the mass transport as well as for the four other components. It is clear that the pure Stokes-swell component, $|\mathbf{M}_{\mathrm{St}}^{\mathrm{swell}}|$ is about 3 times the value of the wind-sea component, $|\mathbf{M}_{\mathrm{St}}^{\mathrm{sea}}|$. The wind-sea component in the Stokes-Ekman interaction term $|\mathbf{M}_{\mathrm{St-Ek}}^{\mathrm{sea}}|$ is about $4 - 5$ times larger than the swell component, $|\mathbf{M}_{\mathrm{St-Ek}}^{\mathrm{swell}}|$. This result is in agreement with the fact that the Stokes-Ekman interaction is mostly due to the interaction between local wind and waves induced Stokes drift.

## 5. Conclusions

In this work the wind induced energy and mass flux have been estimated for the Western Mediterranean Sea from model data. Both magnitudes have been integrated along the Ekman-Stokes layer and spatially and seasonally analyzed. The impact of the Stokes drift depends primarily on two aspects: first, the wind variability at the ocean surface (wave generation) and, second, the geographical configuration of the basin, *i.e.* size, depth and coastline profile (wave propagation), which are particularly complex in the Mediterranean basin.

In the Western Mediterranean Sea, wind induced energy and mass transport along the Ekman-Stokes layer show a marked seasonal character, being higher during winter since wind is stronger and reduced to one half during summer. In the north side of the basin, around the Gulf of Lions, there is a well known cyclogenetic area where high waves are generated mainly during late fall and winter. On the other hand along the coast of North Africa the Stokes transport is higher, being primarily composed by the swell components. At basin level, the Stokes-Ekman mass transport interaction term is about a $10\% - 15\%$ of the total transport but largely depending on the spatial location

The main drawback of this work is related to the statistical wave magnitudes and the empirical parametrizations applied, the assumption of stationarity and the unavailability of the full wave spectra, the use of a constant eddy viscosity model and the ageostrophy of the currents. However, our results can be taken as a lower bound of the magnitudes presented. In addition, to solve the corrected Stokes depth requires considerable computational effort since they were estimated for hundreds of grid points and thousands of days. The different contributions from the swell and wind-sea components are analyzed by assuming that they can be linearly decomposed. The total mass transport following this decomposition is 10% higher.

Results emphasize the importance of including the Stokes drift in the estimation of the upper ocean transports. Inclusion of the Stokes-wind interaction terms is specially important for operational applications aimed to provide forecasts for oil spill and Search and Rescue operations. Neglecting those terms can result in errors in the surface velocity around 40% of the wind induced velocity, and the magnitude can be even higher than the geostrophic velocities obtained from altimetry. Another remarkable point is the role that, at local level, Stokes transport terms, mainly the swell component, can play in accumulating floating debris. The North of Africa, specially Algeria, but also Morocco, Tunisia and the South of Spain have been found to be sinks of marine debris. Other mechanisms for debris transport such as the advection by Langmuir circulation can also be included for a better understanding of the fate of pollutants at the subbasin scale.

Despite some previous studies about the role of the Stokes drift in the wind induced energy and momentum distribution, to our knowledge, this is the first time that it has been studied with some detail in the Mediterranean Sea.



## Acknowledgments

JMS is supported by the PhD CSIC-JAE program co-funded by the European Social Fund (ESF). AO thanks support from the ENAP-Colombian

Army. Financial support EU-H2020 Project Jerico-Next is greatly acknowledged. Authors are indebted to Dr. Biel Jordà for providing the wave model data and Puertos del Estado for the buoy data. We would like to thank comments from 4 anonymous referees which helped to improve significantly the original Manuscript.

## Appendix 1

In the Table 1 are displayed the following statistical magnitudes, being $\mathrm{M_i}$ and $\mathrm{O_i}$ are the model and real (buoy) observations respectively. N is the data length. The Scatter Index (S.I.) [%] is defined as,

$$\mathrm{SI} = \frac{1}{\mathrm{O_{RMS}}} \left[ \frac{1}{\mathrm{N}-1} \sum_{\mathrm{i}=1}^{\mathrm{N}} \left( \mathrm{M_i} - \bar{\mathrm{M}} - (\mathrm{O_i} - \bar{\mathrm{O}}) \right)^2 \right]^{\frac{1}{2}}. \tag{18}$$

The Normalized mean Bias NB is,

$$\mathrm{NB} = 100\% \times \frac{\sum_{i=1}^{N} (\mathrm{M_i} - \mathrm{O_i})}{\sum_{i=1}^{N} \mathrm{O_i}}. \tag{19}$$

The Root Mean Square Error (RMSE) between observations and model is:

$$\mathrm{RMSE} = \left[ \frac{1}{\mathrm{N}} \sum_{\mathrm{i}=1}^{\mathrm{N}} (\mathrm{M_i} - \mathrm{O_i})^2 \right]^{1/2}. \tag{20}$$

The Correlation Coefficient (CC) is calculated as:

$$\mathrm{CC} = \frac{1}{\mathrm{N}-1} \sum_{\mathrm{i}=1}^{\mathrm{N}} \left( \frac{\mathrm{M_i} - \bar{\mathrm{M}}}{\sigma_{\mathrm{M_i}}} \right) \left( \frac{\mathrm{O_i} - \bar{\mathrm{O}}}{\sigma_{\mathrm{O_i}}} \right) \tag{21}$$

where

$$\mathrm{O_{RMS}} = \left[ \frac{1}{\mathrm{N}} \sum_{i=1}^{\mathrm{N}} (\mathrm{O_i})^2 \right]^{1/2}. \tag{22}$$

Ardhuin, F., Mari, L., Rascle, N., Forget, P., Roland, A., 2009. Observation and Estimation of Lagrangian, Stokes, and Eulerian Currents Induced by Wind and Waves at the Sea Surface. J. Phys. Oceanogr. 39 (11), 2820–2838.

Bidlot, J.-R., 2001. ECMWF wave model products. Newsletter. Reading, United Kingdom: 91, 9–15.

Breivik, Ø., Janssen, P. A. E. M., Bidlot, J.-R., 2014. Approximate Stokes Drift Profiles in Deep Water. J. Phys. Oceanogr. 44 (9), 2433–2445.

Carrasco, A., Semedo, A., Isachsen, P., Christensen, K., Saetra, O., 2014. Global surface wave drift climate from ERA-40: the contributions from wind-sea and swell. Ocean Dynamics 64, 1815–1829.

Csanady, G., 1982. Circulation in the coastal ocean. D. Publishing Reidel Company.

D'Ortenzio, F., Iudicone, D., de Boyer Montegut, C., Testor, P., Antoine, D., Marullo, S., Santoleri, R., Madec, G., 2005. Seasonal variability of the mixed layer depth in the Mediterranean Sea as derived from in situ profiles. Geophys. Res. Lett. 32, L12605.

Ekman, V. W., 1905. On the influence of the Earth's rotation on ocean currents. Arch. Math. Astron. Phys. 2, 1–52.

Harcourt, R. R., DAsaro, E. A., 2008. Large eddy simulation of Langmuir turbulence in pure wind seas. J. Phys. Oceanogr., 38, 15421562.

Kantha, L., Wittmann, P., Sclavo, M., Carniel, S., 2009. A preliminary estimate of the Stokes dissipation of wave energy in the global ocean. Geophys. Res. Lett. 36 (2), L02605.

Komen, G. J., Cavaleri, L., Donelan, M., Hasselmann, K., Hasselmann, S., Janssen, P. A. E. M., 1994. Dynamics and Modelling of Ocean Waves. Cambridge University Press, UK.

Kubota, M., 1994. A mechanism for the accumulation of floating marine debris north of Hawaii. Journal of Physical Oceanography 5 (24), 1059–1064.

Lewis, D., Belcher, S., 2004. Time-dependent, coupled, Ekman boundary layer solutions incorporating Stokes drift. Dynamics of Atmospheres and Oceans 37 (4), 313 – 351.

Li, M., Garrett, C., 1993. Cell merging and the jet/downwelling ratio in Langmuir circulation. Journal of Marine Research 51 (4), 737–769.

Liu, B., Wu, K., Guan, C., 2007. Global estimates of wind energy input to subinertial motions in the Ekman-Stokes layer. Journal of Oceanography 63 (3), 457–466.

Liu, G., Perrie, W. A., He, Y., 2014. Ocean surface Stokes drift from scatterometer observations. International Journal of Remote Sensing 35 (5), 1966–1978.

Longuet-Higgins, M. S., 1953. Mass transport in water waves. Philosophical Transactions of the Royal Society of London A: Mathematical, Physical and Engineering Sciences 245 (903), 535–581.

Martínez-Asensio, A., Marcos, M., Jorda, G., Gomis, D., 2013. Calibration of a new wind-wave hindcast in the Western Mediterranean. Journal of Marine Systems 121-122 (7), 1 – 10.

McWilliams, J. C., Restrepo, J. M., 1999. The wave-driven ocean circulation. J. Phys. Oceanogr., 29, 2523–2540.

McWilliams, J. C., Huckle, E., Liang, J., Sullivan, P. P., 2013. Langmuir Turbulence in Swell. J. Phys. Oceanogr. 44 (3), 870–890.

McWilliams, J. C., Sullivan, P. P., Moeng, C. H., 1997. Langmuir turbulence in the ocean. J. Fluid Mech., 334, 1–30.

McWilliams, J. C., Restrepo, J. M., Lane, E. M., 2004. An asymptotic theory for the interaction of waves and currents in coastal waters. J. Fluid Mech., 511, 135–178.

Mellor, G. L., 2008. The depth-dependent current and wave interaction equations: A revision. J. Phys. Oceanogr., 38, 2587–2596.

Nimmo Smith, W. A. M., Thorpe, S.A., 1999. Dispersion of Buoyant Material by Langmuir Circulation and a Tidal Current. Marine Pollution Bulletin 38 (9), 824–829.

Polton, J., 2009. A wave averaged energy equation: Comment on “global estimates of wind energy input to subinertial motions in the Ekman-Stokes layer” by Bin Liu, Kejian Wu and Changlong Guan. Journal of Oceanography 65 (5), 665–668.

Polton, J. A., Lewis, D. M., Belcher, S. E., 2005. The Role of Wave-Induced Coriolis-Stokes Forcing on the Wind-Driven Mixed Layer. J. Phys. Oceanogr. 35 (4), 444–457.

Ponce de León, S., Orfila, A., Simarro, G., 2016. Wave energy in the Balearic Sea. Evolution from a 29 year spectral wave hindcast. Renewable Energy 85, 1192 – 1200.

Pond, S., Pickard, G., 1983. Introductory dynamical oceanography, 2nd Edition. Pergamon international library of science, technology, engineering, and social studies. Pergamon Press.

Poulain, P.-M., Menna, M., Mauri, E., 2012. Surface Geostrophic Circulation of the Mediterranean Sea Derived from Drifter and Satellite Altimeter Data. Journal of Physical Oceanography 42, 973–990.

Smith, J., 2006. Wave-current interactions in finite depth. J. Phys. Oceanogr., 36, 1403–1419.

Stokes, G., 1847. On the theory of oscillatory waves. Transactions of the Cambridge Philosophical Society 8, 441–455.

Tamura, H., Miyazawa, Y., Oey, L.-Y., 2012. The Stokes drift and wave induced-mass flux in the North Pacific. Journal of Geophysical Research: Oceans 117 (C8021), 1–14.

Teixeira, M. A. C., 2012. The influence of Langmuir turbulence on the scaling for the dissipation rate in the oceanic boundary layer. Journal of Geophysical Research: Oceans 117 (C5).

Thorpe, S. A., 2009. Spreading of floating particles by Langmuir circulation. Marine Pollution Bulletin 58, 1787–1791.

Uchiyama, Y. J. C., McWilliams, J. C., Shchepetkin, A.F., 2010. Wave-current interaction in an oceanic circulation model with a vortex force formalism: Application to the surf zone. Ocean Modell., 34, 16–35.

Weber, J. E. H., Brostrom, G., Saetra, O., 2006. Eulerian versus Lagrangian approaches to the wave-induced transport in the upper ocean. J. Phys. Oceanogr., 36, 2106–2118.

Wu, K., Liu, B., 2008. Stokes driftinduced and direct wind energy inputs into the Ekman layer within the Antarctic Circumpolar Current. Journal of Geophysical Research: Oceans 113 (C10002), 1–12.

686 ## 6. Tables

| Buoy | Method | GAP | Mean (cm/s) | CC | NB | SI | RMSE |
|---|---|---|---|---|---|---|---|
| | | (%) | (buoy, model) | | (%) | (%) | (cm/s) |
| Cabo Begur | Bulk cal. | 33.6 | (– – ,3.81) | 0.7 | 17.2 | 69.5 | 1.82 |
| | Bulk noncal. | – | (3.21,2.40) | 0.81 | -26.9 | 40.9 | 1.61 |
| | Ardh. cal. | – | (– – ,5.28) | 0.9 | -2.4 | 33.4 | 1.65 |
| | Ardh. noncal. | – | (4.92,4.53) | 0.9 | -15.5 | 33.5 | 1.73 |
| Cabo Palos | Bulk cal. | 29.0 | (– – ,3.37) | 0.62 | 47.3 | 63.2 | 1.84 |
| | Bulk noncal. | – | (2.27,2.03) | 0.72 | -11.8 | 46.8 | 1.21 |
| | Ardh. cal. | – | (– – ,3.51) | 0.88 | 11.4 | 35.6 | 1.53 |
| | Ardh. noncal. | – | (3.75,2.93) | 0.88 | 5.3 | 35.2 | 1.49 |
| Dragonera | Bulk cal. | 3.3 | (– – ,2.71) | 0.53 | 18.2 | 64.3 | 1.93 |
| | Bulk noncal. | – | (2.32,1.61) | 0.64 | -30.0 | 50.2 | 1.62 |
| | Ardh. cal. | – | (– – , 3.51) | 0.87 | -3.4 | 32.9 | 1.59 |
| | Ardh. noncal. | – | (3.61,2.93) | 0.87 | -19.5 | 33.2 | 1.74 |
| Cabo Gata | Bulk cal. | 4.6 | (– – ,2.31) | 0.56 | -1.2 | 60.9 | 1.87 |
| | Bulk noncal. | – | (2.34,1.38) | 0.67 | -40.0 | 49.9 | 1.78 |
| | Ardh. cal. | – | (– – ,3.18) | 0.86 | -19.5 | 37.4 | 1.86 |
| | Ardh. noncal | – | (3.62,2.62) | 0.85 | -29.9 | 37.7 | 2.07 |
| Maó | Bulk cal. | 40.8 | (– – ,2.90) | 0.58 | 34.1 | 59.2 | 1.27 |
| | Bulk noncal. | – | (2.12,1.74) | 0.69 | -20.78 | 46.9 | 0.97 |
| | Ardh. cal. | – | (– – ,4.52) | 0.87 | -2.4 | 34.7 | 1.59 |
| | Ardh. noncal. | – | (4.62,3.84) | 0.87 | -17.3 | 35.1 | 1.64 |
| Tarragona | Bulk cal. | 6.6 | (– – ,2.51) | 0.56 | 9.3 | 65.7 | 1.98 |
| | Bulk noncal. | – | (2.32, 1.47) | 0.64 | -35.7 | 52.3 | 1.75 |
| | Ardh. cal. | – | (– – ,2.55) | 0.85 | -15.3 | 38.4 | 1.71 |
| | Ardh. noncal. | – | (3.05,2.05) | 0.85 | -31.7 | 38.7 | 1.91 |

Table 1: Statistical estimates for the Stokes drift computed by the bulk expression and Ardhuin (Ardh) parametrization for the buoys and for the calibrated (cal) and raw (noncal) model data. CC (correlation coefficient), NB (normalized mean bias), SI (percentage scatter index) and RMSE (root mean square). The percentage of missing data in each timeseries is provided in the GAP column. The mathematical definitions of the statistical estimators are given in Appendix 1.

Table 2: Stokes e-folding depth comparison.

| **Method** | **Mean** $[m]$ | **Std** $[m]$ | **Median** $[m]$ |
|---|---|---|---|
| Bulk | 3.41 | 2.55 | 2.62 |
| Breivik | 2.80 | 2.07 | 2.12 |

687 ## 7. Figures

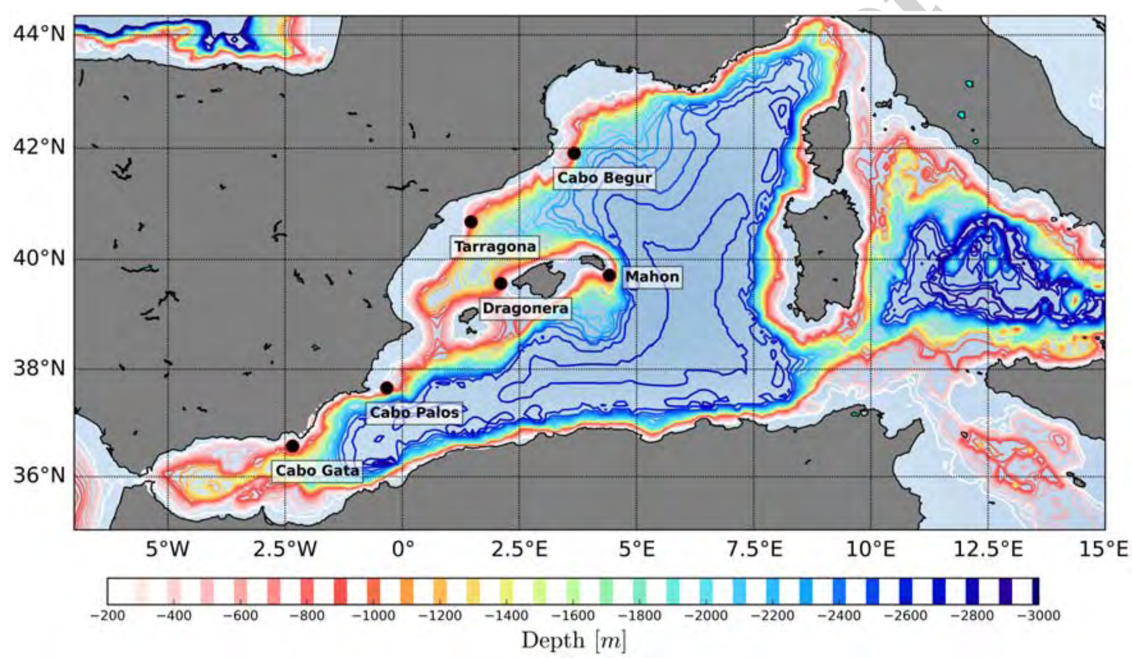


Figure 1: Buoy locations (black circles) and western Mediterranean Sea bathymetry contour map. Units in m.

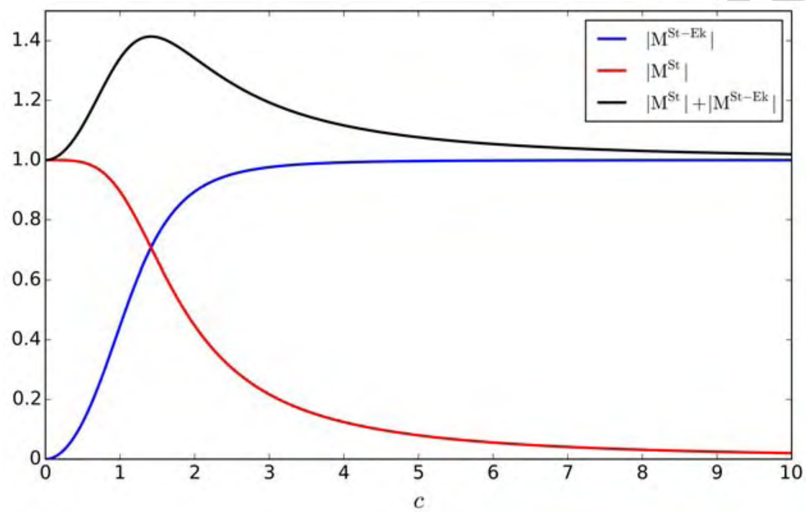


Figure 2: Mass transport modulus for Stokes term (red line), for Stokes-Ekman interaction (blue line) and for the addition of both terms (black line). It has been normalized by $(\delta_{\mathrm{St}}\,\mathrm{U_s})$ as a function of $c = \delta_{\mathrm{Ek}}/\delta_{\mathrm{St}}$.

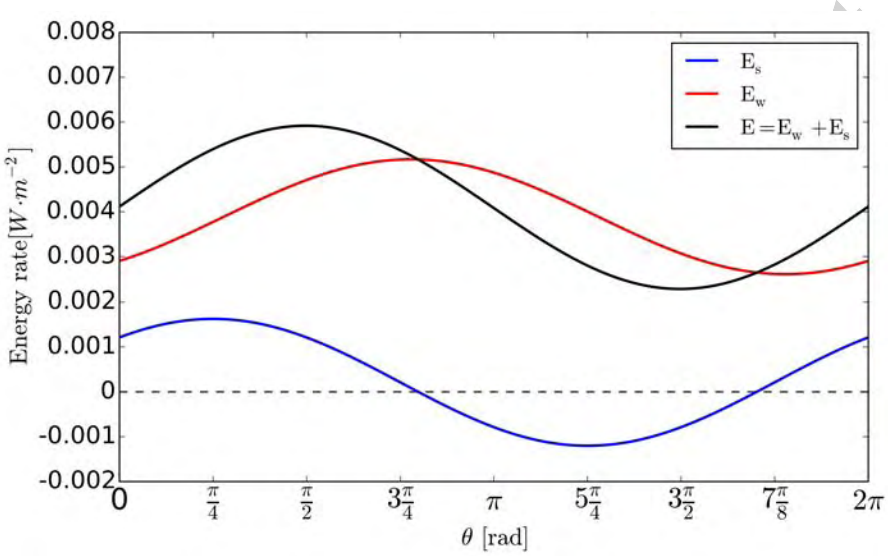


Figure 3: Total wind energy input (E, solid black line) and its redistribution between direct wind-induced energy rate ($E_w$ from Eq. (8), solid red line) and indirect energy rate on wave terms ($E_s$ from Eq. (9), solid blue line). Some parameters and/or variables have are assumed constant: $|\boldsymbol{\tau}_0| = 0.1\,\mathrm{N}\cdot\mathrm{m}^{-2}$, $|\mathbf{U}_{s_0}| = 0.1\,\mathrm{m}\cdot\mathrm{s}^{-1}$, $\delta_{\mathrm{Ek}} = 25\,\mathrm{m}$, $\delta_{\mathrm{St}} = 2.5\,\mathrm{m}$, $c = 10$, $f = 10^{-4}\,\mathrm{s}^{-1}$. $\theta$ is the angle between wind and waves in a clockwise sense. Horizontal black dashed line shows the zero energy line. Units in $\mathrm{W}\cdot\mathrm{m}^{-2}$.

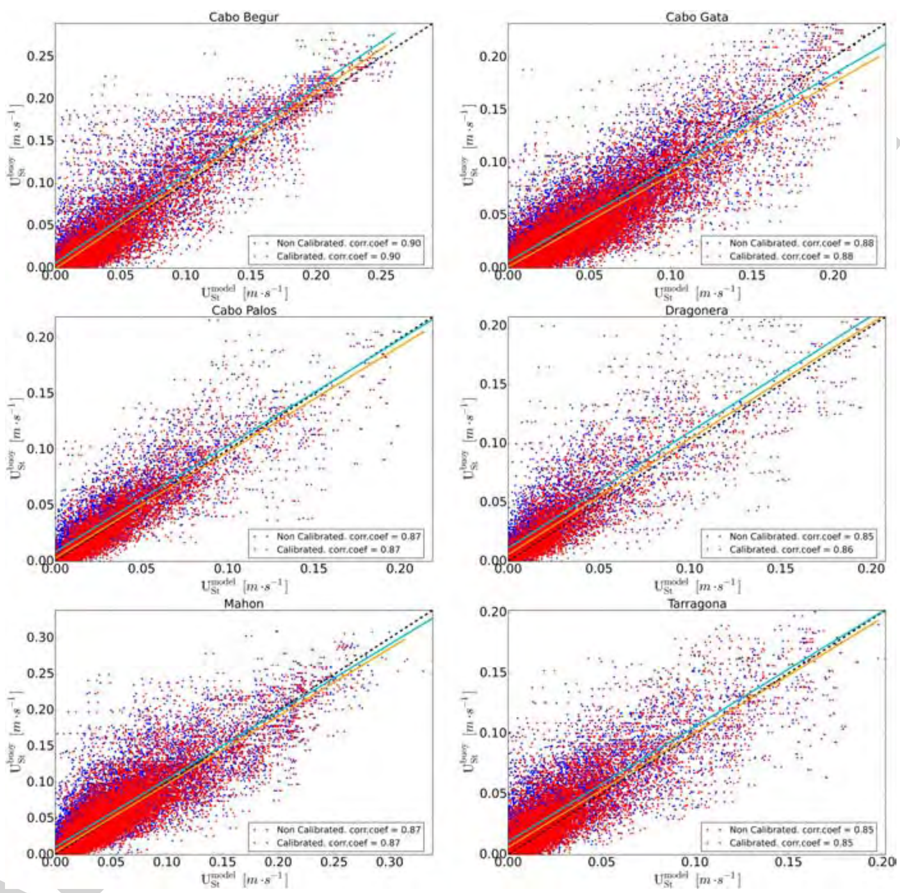


Figure 4: Stokes drift and linear fits, $U_{St}$ computed following Ardhuin et al. (2009) at each buoy for calibrated (red dots and orange solid line) and non calibrated (blue dots and cyan solid line) data as given in Martínez-Asensio et al. (2013).

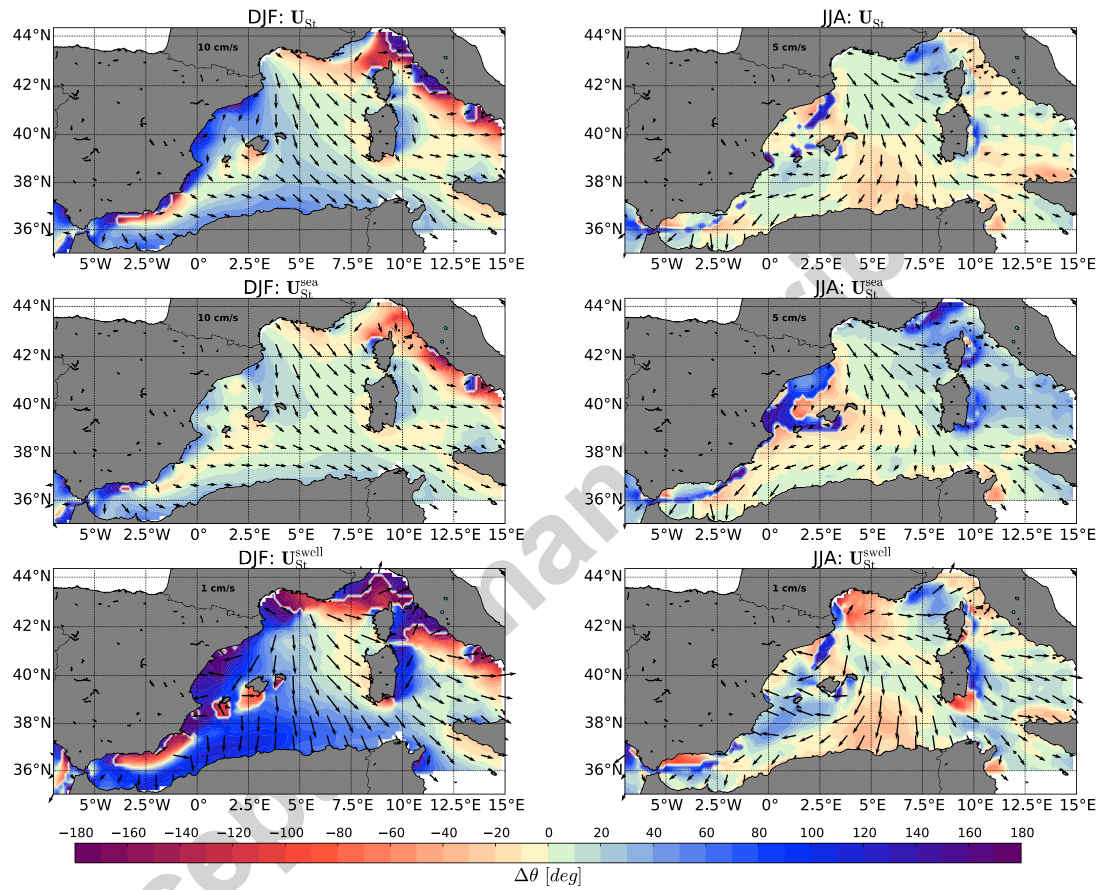


Figure 5: Top row: averaged Stokes drift (black arrows) for DJF (left) and for JJA (right). Central row: averaged wind-sea component for the Stokes drift for DJF (left) and JJA (right). Bottom row: averaged swell component for the Stokes drift for DJF (left) and JJA (right). Vector length units in $\mathrm{cm} \cdot \mathrm{s}^{-1}$. Background color represents the angular deviation (in degrees) between the direction of the averaged surface wind field (at 10 m) and the direction of the Stokes drift.

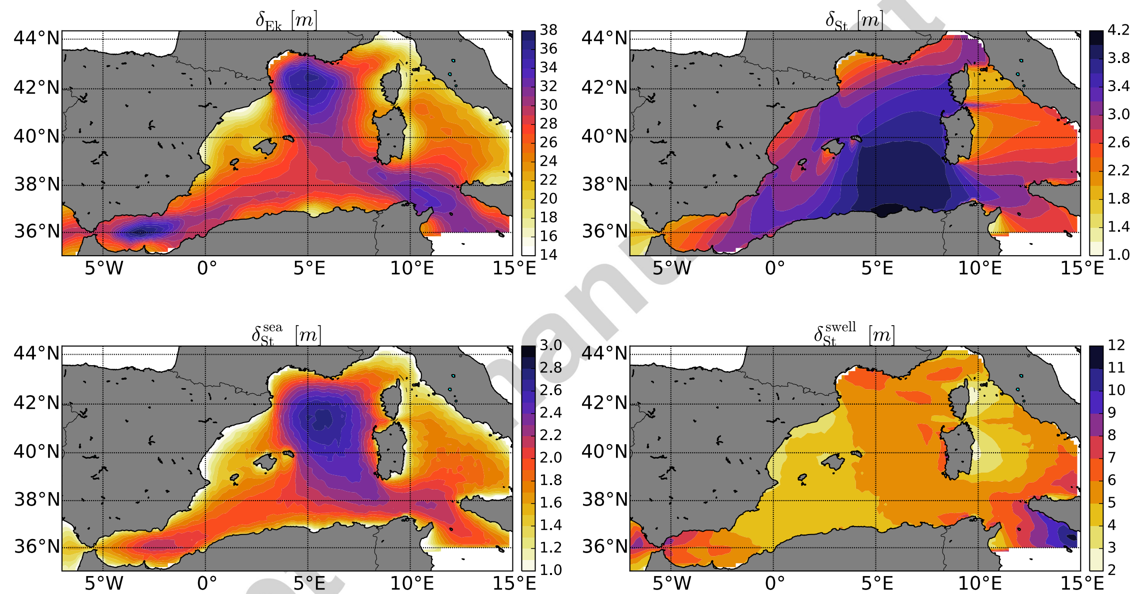


Figure 6: Averaged Ekman depth (top-left). Averaged Stokes depth (top-right). Averaged wind-sea Stokes depth average (bottom-left). Averaged Stokes swell depth average (bottom-right). The Ekman depth is estimated according to Eq. (15) and the Stokes depths by solving Eq. (14). Period extends from 1993 to 2008. Units in m.

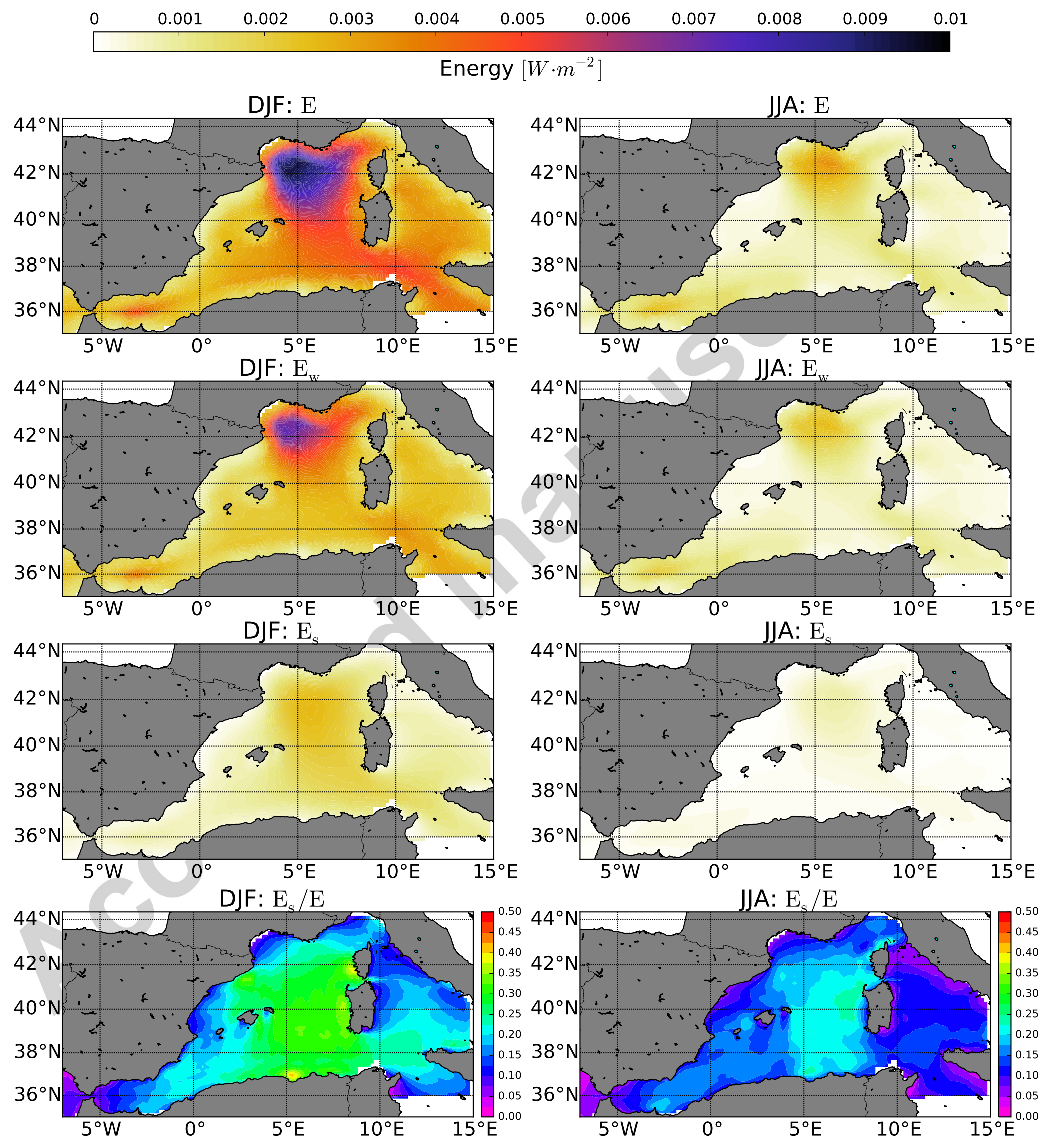




Figure 7: First row: total averaged energy rate. Second row: wind induced averaged energy rate. Third row: wave induced averaged energy rate. Units in $\mathrm{W \cdot m^{-2}}$. Fourth row: ratio between wave induced energy rate and total energy rate. Left column for DJF and right column for JJA.

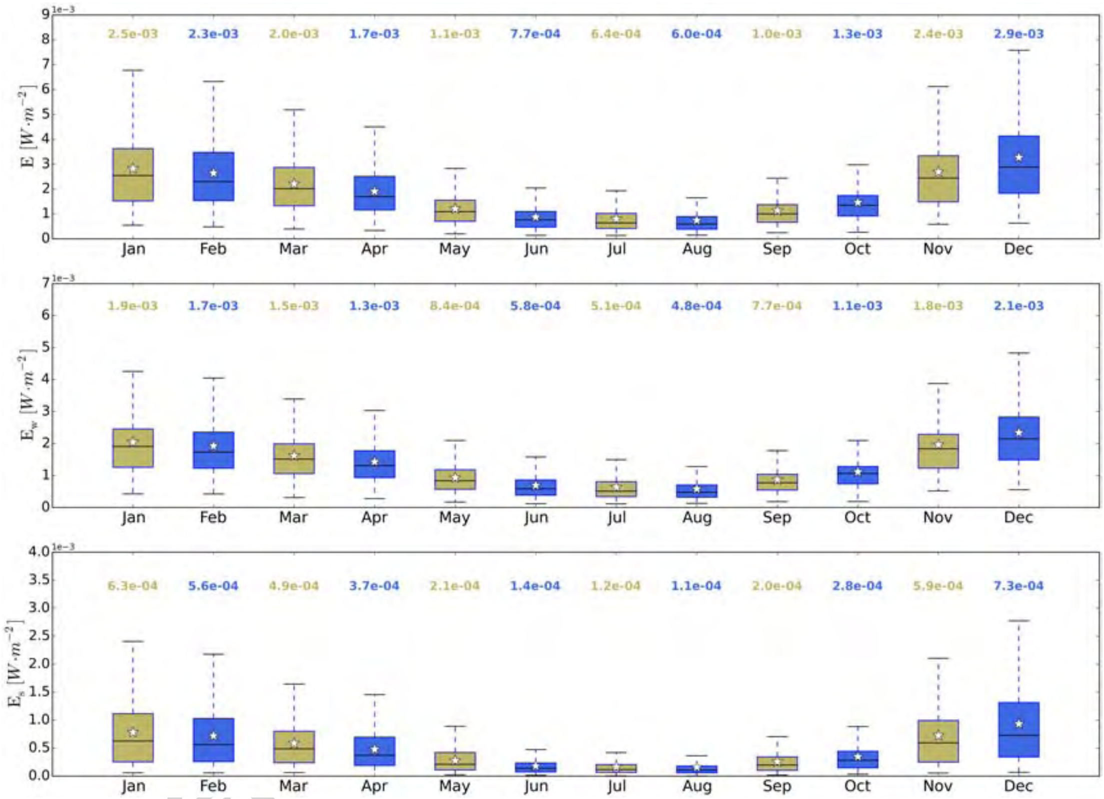


Figure 8: Top panel: box plot of monthly spatially averaged total energy rate. Middle panel: monthly spatially averaged wind induced energy rate. Bottom panel: monthly spatially averaged wave induced energy rate. Stars represent the mean value and the number on each box the median. Each box represents the interquartile range: $Q_1$ (percentile $25^{\rm th}$) to $Q_3$ (percentile $75^{\rm th}$) and upper and bottom whiskers are computed as: $Q_3 + 1.5 \cdot (Q_3 - Q_1)$ and $Q_1 - 1.5 \cdot (Q_3 - Q_1)$ respectively. Units in $\mathrm{W \cdot m^{-2}}$.

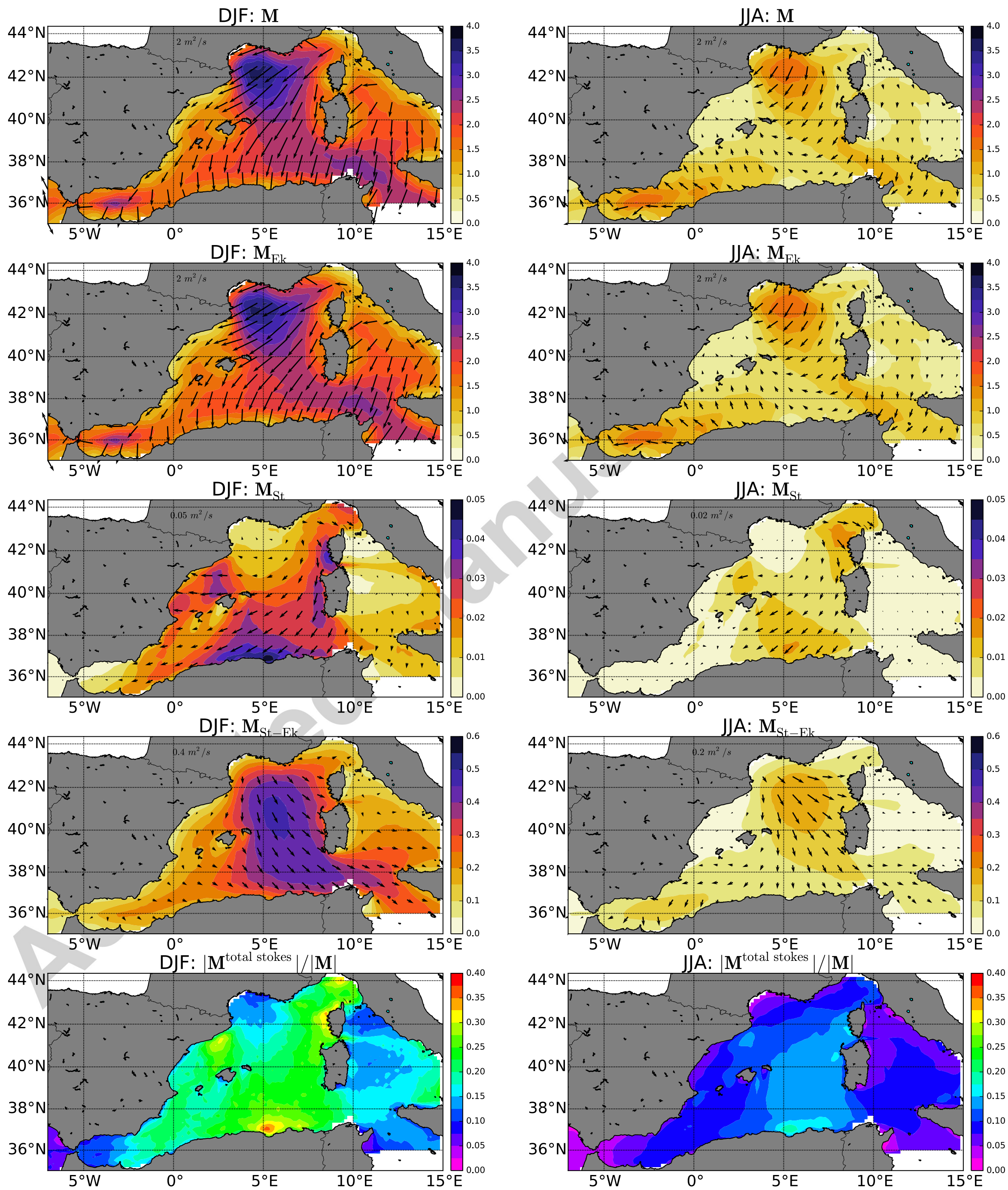


Figure 9: First row: vertically integrated total mass flux. Second row: vertically integrated Ekman mass flux. Third row: vertically integrated Stokes mass flux. Fourth row: vertically integrated Stokes-Ekman interaction mass flux. Units in $\mathrm{m}^2 \cdot \mathrm{s}^{-1}$. Fifth row: median ratio between Stokes related mass transport (which is the addition of both, the pure Stokes and the Stokes-Ekman interaction term) and the total mass transport. Left column for DJF and right column for JJA.

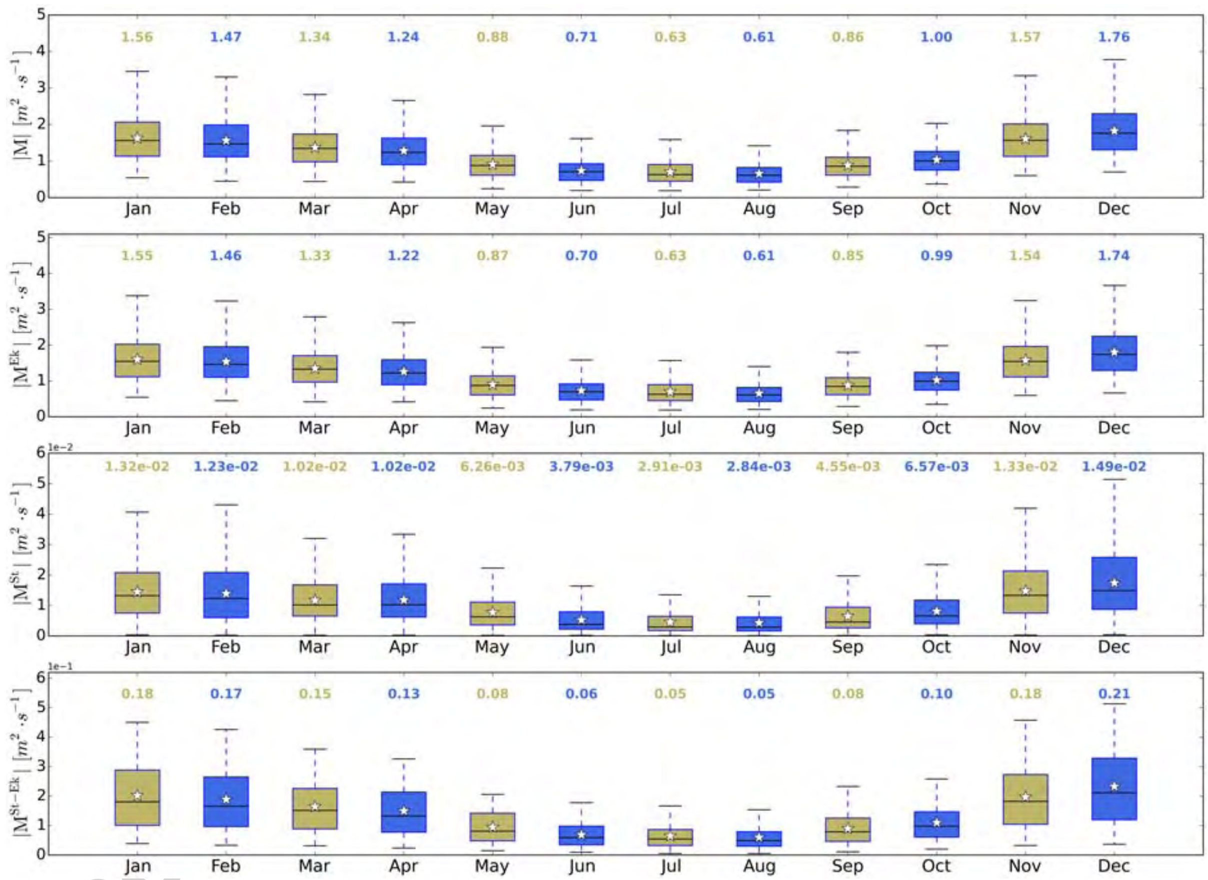


Figure 10: First panel: box plot of the modulus of the monthly spatially averaged total mass transport. Second panel: modulus of the monthly spatially averaged Ekman mass transport. Third panel: modulus of the monthly spatially averaged Stokes. Fourth panel: modulus of the monthly spatially averaged Stokes-Ekman interaction mass transport. The numbers, symbols and box-plot quantiles are the same as in Figure 8.

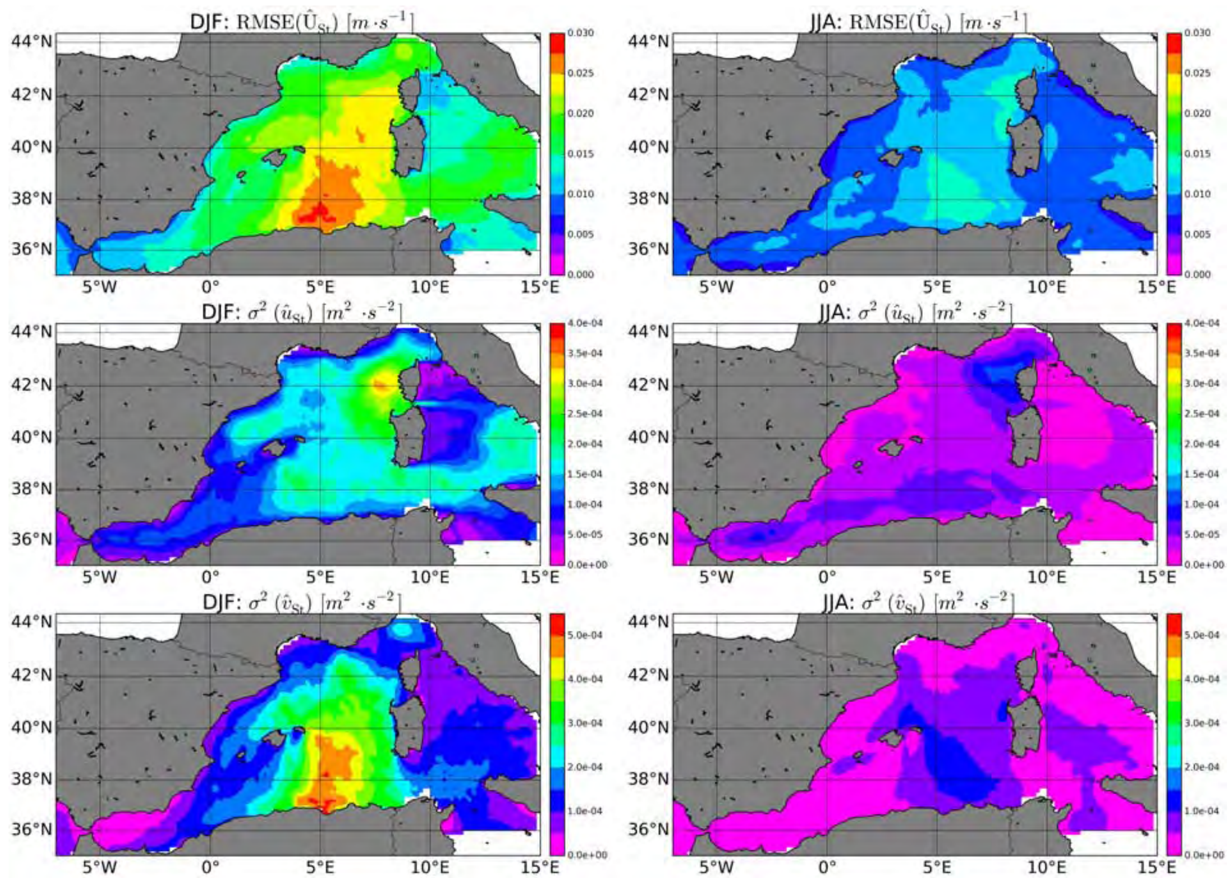


Figure 11: Top panels present the Stokes drift velocity Root Mean Square Error (for total velocity). Middle and bottom panels show the variance ($u$ and $v$ components respectively). Left column for winter season (DJF), right column for summer (JJA). RMSE = $\sqrt{\frac{1}{n_t}\sum_{i=1}^{n_t}(\hat{u}_{\mathrm{St}})^2 + (\hat{v}_{\mathrm{St}})^2}$, being $\hat{u}_{\mathrm{St}} = u_{\mathrm{St}} - (u_{\mathrm{St}}^{\mathrm{sea}} + u_{\mathrm{St}}^{\mathrm{swell}})$ and $\hat{v}_{\mathrm{St}} = v_{\mathrm{St}} - (v_{\mathrm{St}}^{\mathrm{sea}} + v_{\mathrm{St}}^{\mathrm{swell}})$. Units in $\mathrm{m} \cdot \mathrm{s}^{-1}$ for RMSE and $\mathrm{m}^2 \cdot \mathrm{s}^{-2}$ for variance.

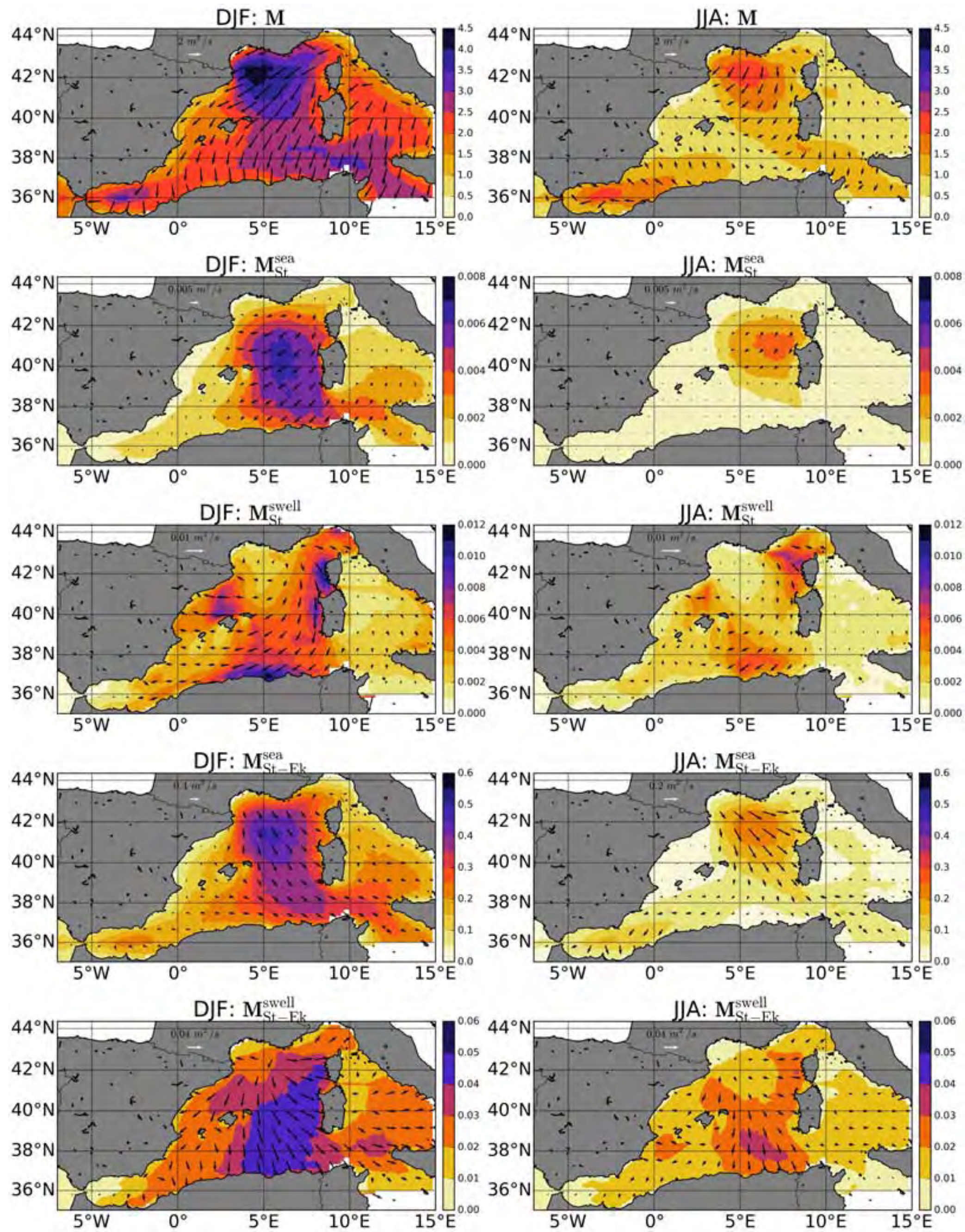




Figure 12: Mass depth integrated transport average along the Ekman-Stokes layer decomposing the Stokes drift velocity in wind-sea and swell components. The first row panels represent the total transport average in winter (DJF) and summer (JJA). The second row panels show the pure Stokes wind-sea transport. The third row panels the pure Stokes swell induced mass transport. The fourth row panels the Stokes-Ekman interaction wind-sea ea term. The last row is the Stokes-Ekman interaction swell component term.

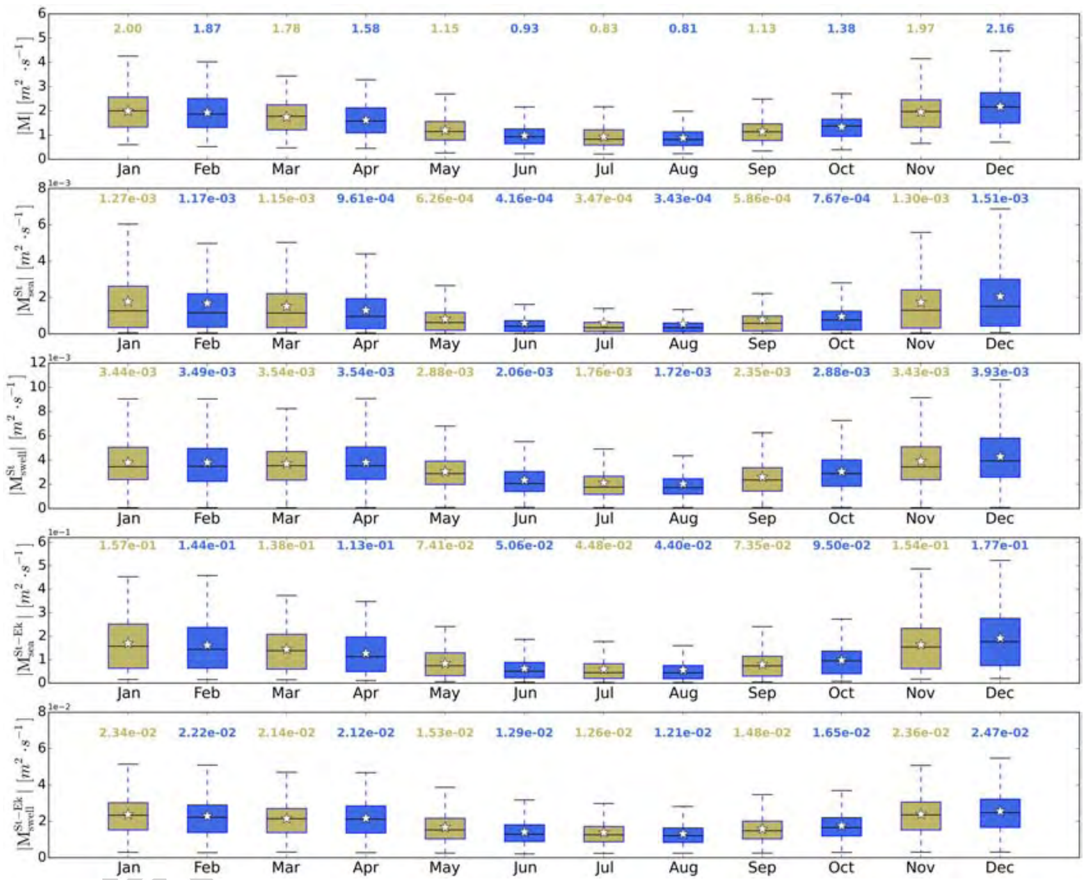


Figure 13: First panel: box plot of the modulus of the monthly spatially averaged total mass transport. Second panel: modulus of the monthly spatially averaged pure Stokes wind-sea component. Third panel: modulus of the monthly spatially averaged pure Stokes swell term. Fourth panel: modulus of the monthly spatially averaged Stokes-Ekman interaction wind-sea mass transport. Fifth panel: modulus of the monthly spatially averaged Stokes-Ekman interaction swell component. The numbers, symbols and box-plot quantiles are the same as in Figure 8.